High-Speed Video Microscopy in Optical Tweezers

Stephen Alexander Juhani Keen

BSc, MSc

Submitted in fulfilment of the requirements
for
the Degree of PhD

Department of Physics & Astronomy
Faculty of Physical Sciences
University of Glasgow

November 9, 2009

Abstract

Optical tweezers have become an invaluable tool for measuring and exerting forces in the pico-Newton regime. Force measurements have in the past concentrated on using only one trapped particle as a probe, partly due to the difficulties in tracking more than one particle at high enough frame rate. Recent advances in video camera technology allow the collection of images at several kHz. However, there has been little use of high-speed cameras in optical tweezers, partly due to data management problems and affordability. This thesis presents seven experiments carried out during my PhD involving the use of several different high-speed cameras.

Chapter 3 presents the use of a CMOS high-speed camera with integrated particle tracking built by Durham Smart Imaging. The camera was used in a Shack-Hartmann sensor setup to determine rapidly and non-ambiguously the sign and magnitude of the orbital angular momentum of a helically-phased beam light beam, as an alternative to interferometric techniques. Chapter 4 presents a direct comparison of a CCD high-speed video camera with a quadrant photodiode to track particle position. Particle tracking was possible at high enough accuracy and bandwidth to allow convenient trap calibration by thermal analysis. Chapter 5 reports an investigation of the resulting change in trap stiffness during the update of trap positions in holographic optical tweezers. Chapter 6 presents the results from using a high-speed camera to successfully track multiple particles in a microfluidic channel to measure the viscosity at several points simultaneously. The last three chapters investigate the hydrodynamic interactions between trapped particles under different conditions and comparisons were made with theory.

Author's Declaration

I hereby declare that this thesis is the result of my own work, except where explicit reference is made to the work of others, and has not been presented in any previous application for a degree at this or any other institution.

.....

Stephen Keen

Publications

Presented in Thesis

S. A. J. Keen, A. M. Yao, J. Leach, R. Di Leonardo, C. D. Saunter, G. D. Love, J. Cooper, M. J. Padgett. Multipoint viscosity measurements in microfluidic channels using optical tweezers. *Lab on a Chip* **9**, 2059-2062, 2009.

A. M. Yao, S. A. J. Keen, D. Burnham, J. Leach, R. Di Leonardo, D. McGloin, M. J. Padgett. Demonstration of underdamped modes in a damped system of hydrodynamically coupled microparticles. *New Journal of Physics* **11**, 053007, 2009.

R. Di Leonardo, S. Keen, F. Ianni, J. Leach, M. J. Padgett, G. Ruocco. Hydrodynamic Interactions in Two Dimensions. *Phys. Rev. E* **78**, 031406, 2008.

E. Eriksson, S. Keen, J. Leach, M. Goksr, M. J. Padgett. The effect of external forces on discrete motion within holographic optical tweezers. *Opt. Express* **15**, 18268-18274, 2007.

R. Di Leonardo, S. Keen, J. Leach, C. D. Saunter, G. D. Love, G. Ruocco, M. J. Padgett. Eigenmodes of a hydrodynamically coupled micron-size multiple-particle ring. *Phys. Rev. E* **76**, 061402, 2007.

S. Keen, J. Leach, G. Gibson, M. J. Padgett. Comparison of a high-speed

camera and a quadrant detector for measuring displacements in optical tweezers. *J. Opt. A: Pure Appl. Opt.* **9**, S264-S266, 2007.

J. Leach, S. Keen, M. J. Padgett, C. Saunter, G. D. Love. Direct measurement of the skew angle of the Poynting vector in a helically phased beam. *Opt. Express* **14**, 11919-11924, 2006.

Other Publications

G. M. Gibson, J. Leach, S. Keen, A. J. Wright M. J. Padgett. Measuring the accuracy of particle position and force in optical tweezers using high-speed video microscopy. *Opt. Express* **16**, 14561-14570, 2008.

D. Preece, S. Keen, E. Botvinick, R. Bowman, J. Leach, M. J. Padgett. Independent polarization control of multiple optical traps. *Opt. Express* **16**, 15897-15902, 2008.

J. Leach, H. Mushfique, S. Keen, R. Di Leonardo, G. Ruocco, J.M. Cooper, and M.J. Padgett. Comparison of Faxén's correction for a microsphere translating or rotating near a surface. *Phys. Rev. E* **79**, 026301, 2009.

Contents

List of Figures

Acknowledgements

I would like to give a big thank you to Miles Padgett for being such an enthusiastic and supportive supervisor. I am also very thankful to Roberto Di Leonardo for allowing me to work with him at Rome University and making me feel very welcome during my stay. I would like to acknowledge and thank Chris Saunter and Gordon Love at Durham University for their collaboration and help during the use of their 'Smart Camera' technology in several experiments. Thankyou also to Emma Eriksson and Mattias Goksör from Gothenberg University for visiting the group and collaborating with us. Thankyou to the whole of the Optics Group for the friendship over the years and for helping to proof-read my thesis! In particular I am indebted to Graham Gibson, Jonathan Leach and Alison Yao, who I worked closely with and constantly bugged for help and advice; thankyou for your patience. Finally, I wish to thank my family and friends 'down South', without their encouragement this thesis would not have been possible.

This research is supported by the Engineering and Physical Sciences Research Council (EPSRC)

CHAPTER 1

Introduction

One of the first references to the possibility of light exerting force was made in relation to the direction the tails of comets point. Tycho Brahe, a Danish astronomer, took meticulous measurments of The Great Comet of 1577, noting that the comet's tail consistently pointed away from the Sun. An illustration of The Great Comet is show in figure 1.1 by Jiri Daschitzky. Later, Brahe collaborated with Johannes Kepler to discover that comets' tails *always* point away from the Sun; suggesting the Sun exerted a radiant pressure [2]. This lead to Kepler, in 1611, writing a science fiction book proposing sailing from the Earth to the Moon on light itself. Although a fictional proposition, Kepler's initial ideas are based on reality; light is now used routinely to exert forces on objects.

Almost 400 years later, Arthur Ashkin, in the late 1960's, observed micron-sized dielectric particles experiencing a force due to a focussed laser beam, [3]. When a laser beam was incident on particles of higher refractive index than the surrounding medium, the particles moved along the beam propagation direction as well as towards the center of the beam-axis. This enabled the optical guiding of particles along laser beams, which Ashkin demonstrated in both a liquid and air. Ashkin also achieved full three-

Figure 1.1: The Great comet of 1577, seen over Prague on November 12. Engraving made by Jiri Daschitzky.

dimensional confinement of particles, 1st by using counterpropagating laser beams and later, by using just a single sharply focussed laser beam. Since then optical tweezers have become a useful tool for atom trapping [4] and for manipulating micron-sized particles, including cells [5]. They have particularly found applications in biology and colloid science, where optically trapped particles can be used to apply or measure forces ranging from the femto- to pico-Newton regime [6, 7, 8, 9, 10, 11, 12]. The pico-Newton regime is particularly delicate and diffcult to probe with other micromanipulation tools such as atomic force microscopes [13, 14, 15].

1.1 Thesis format

Chapter 2 explains the principles behind optical tweezers and how they are constructed and calibrated. There is also a brief introduction to holographic

optical tweezers and the difficulties in tracking multiple particles.

Chapter 3 is based on published work [16], presenting the use of a "'smart camera"' with integrated particle tracking built by Durham Smart Imaging. The experiment was carried out at Durham University by myself, Jonathan Leach, Chris Saunter and Gordon Love. A spatial light modulator and Shack-Hartmann lenslet array are used to determine the local skew angle of the Poynting vector within a helically-phased beam. This experiment highlighted the potential of such a camera in an optical tweezers setup, resulting in the camera being modified by Durham Smart Imaging for later use in optical tweezers.

Chapter 4 presents in this chapter a brief demonstration of the feasibility of using a high-speed CCD camera to measure particle positions by collecting positional data from the camera and a quadrant photodiode QPD simultaneously. This experiment was carried out primarily by myself with help and advice from Jonathan Leach and Graham Gibson. This work was subsequently published [17].

Chapter 5 presents published work [18] of an experiment I undertook with Emma Eriksson and Mattias Goksör from Gothenberg University, and Jonathan Leach, to investigate the resulting change in trap stiffness during the update of trap positions in holographic optical tweezers.

Chapter 6 presents results of an experiment I undertook with Alison Yao with help from Jonathan Leach, Roberto Di Leonardo and Jon Cooper to use the Durham Smart Imaging 'smart camera' to track multiple particles, thus allowing viscosity measurements at multiple points within a sample. This work has recently been published.

In Chapter 7 an introduction is given to hydrodynamic interactions between colloidal particles, followed by the details of an experiment I carried out with Dan Burnham (University of St Andrews) and David McGloin (University of Dundee). The hydrodynamic interactions between two closely trapped

water droplets was investigated and its analysis was primarily carried out by Alison Yao. This work has recently been published.

Chapter 8 presents a summary of published work [19] I carried out on a placement at Rome University "La Sapienza" with collaborators Roberto Di Leonardo and Giancarlo Ruocco. Experimental work was carried out by myself, Francesca Ianni and Roberto Di Leonardo. The hydrodynamic interactions between colloidal particles confined in a thin soap-film were studied and compared to a derivation of the two-dimensional Oseen tensor (analysis carried out by Roberto Di Leonardo). The reduced dimensions are thought to increase the range of hydrodynamic interactions compared to a bulk fluid, of relevance to diffusion and interactions of proteins in biological membranes.

Chapter 9 demonstrates the use of the "smart camera" to track the positions of multiple particles held in holographic optical tweezers to detect hydrodynamic coupling between multiple particles. Hydrodynamic coupling between the particles gives a set of eigenmodes, each one independently relaxing with a characteristic decay rate (eigenvalue) that can be measured using our positional data. Experimental work was carried out by myself, Chris Saunter (Durham University) and Jonathan Leach. Results were primarily analysed by Roberto Di Leonardo (Rome University), who compared the experimental results to the predictions of an approximation using the Oseen tensor. This work was published [20].

Finally Chapter 10 concludes with some recent progress in the Optics Group (University of Glasgow) and a summary of the work presented here.

CHAPTER 2

Optical Tweezers

2.1 Introduction

This chapter explains the principles behind optical tweezers and how they are constructed and calibrated. There is also a brief introduction to holographic optical tweezers and the difficulties in tracking multiple particles. Some experimental data collected by myself has been used to illustrate concepts.

A single-beam gradient trap (optical tweezers) can be created by focussing a laser beam to a diffraction-limited spot using a high numerical aperture (NA) objective.

The mechanism behind optical trapping can be explained by various models, which are often limited to either the Rayleigh or Mie regime, where the particle is much smaller or much larger than the wavelength of the trapping beam, respectively. In the Rayleigh regime the particle is treated as a point dipole. In the Mie regime geometric ray optics can be used to explain the force exerted on the particle due to intensity gradient as illustrated in

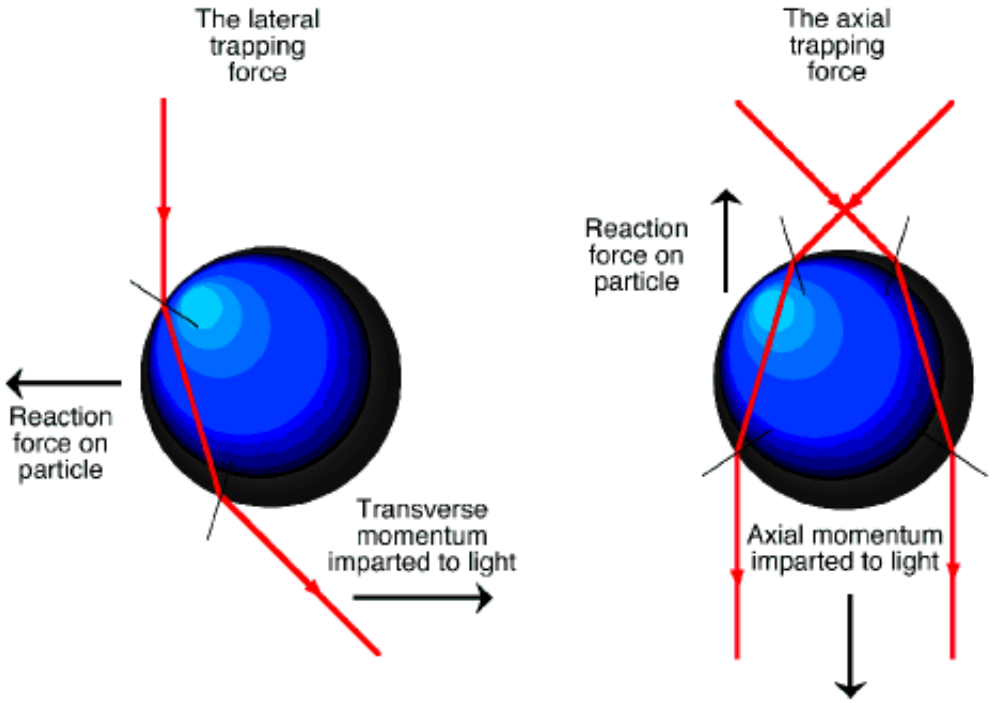

Figure 2.1: The ray optical origin of the lateral and axial trapping force within optical tweezers. When the bead is displaced from the beam center, the refraction of the light rays cause a net force on the particle towards the center of the trap. Courtesy of Molloy and Padgett [21].

Figure 2.1. The particle refracts the light resulting in a reaction force on the particle due to the momentum associated with light. The result of this is that the particle experiences a force directed towards the highest light intensity. The particle also experiences a scattering force from the incident light, directed in the beam propagation direction. When the gradient force is sufficiently high enough to counteract the scattering force then the particle is effectively trapped in the beam focus. For a trapped particle, displacements from the centre of the trap result in a restoring force directed towards the focus, the force directly proportional to the displacement for displacements of less than a particle radius.

2.2 Construction

Typically a microscope objective is used to focus the laser light through a glass coverslip into a sealed sample of fluid where the optical trapping can take place. A high numerical aperture (NA) is required to ensure the gradient force is strong enough to counteract the scattering force, to allow axial trapping (in the beam propagation direction). The NA of the objective is defined by:

$$NA = n \sin \theta \tag{2.1}$$

where n is the index of refraction of the medium in which the lens is working, and θ is the half-angle of the maximum cone of light that can enter or exit the lens. A common optical tweezers setup is show in figure 2.2.

The laser beam is expanded and directed onto a beam-steering mirror $M2$ or diffractive optical element (see later) and then passes through a telescope, consisting of lenses $L3$ and $L4$. A birefringent crystal called a half-wave, which retards one polarization by half a wavelength, can be used to rotate the polarization of the laser beam (which is linearly polarized). By using a suitably orientated half-wave plate and a polarizing beam-splitter, the beam-splitter directs laser light up through the objective. The light from the sample illuminated with a halogen bulb (with a random polarization), passes through the polarizing beam-splitter, to be imaged by $L4$ onto the camera. A filter is placed in front of the camera to prevent any laser light reflected off the coverslip from reaching the camera. The sample is mounted on a motorized stage to enable sample movement in the xy plane. The objective is mounted on a piezo-stage to allow axial (z axis) displacement of the trap within the sample. The trap can be moved laterally in the sample plane by changing the incidence angle of the beam on the objective by using the beam steering mirror, M2, and telescope arrangement (L3 and L4), as shown in figure 2.3.

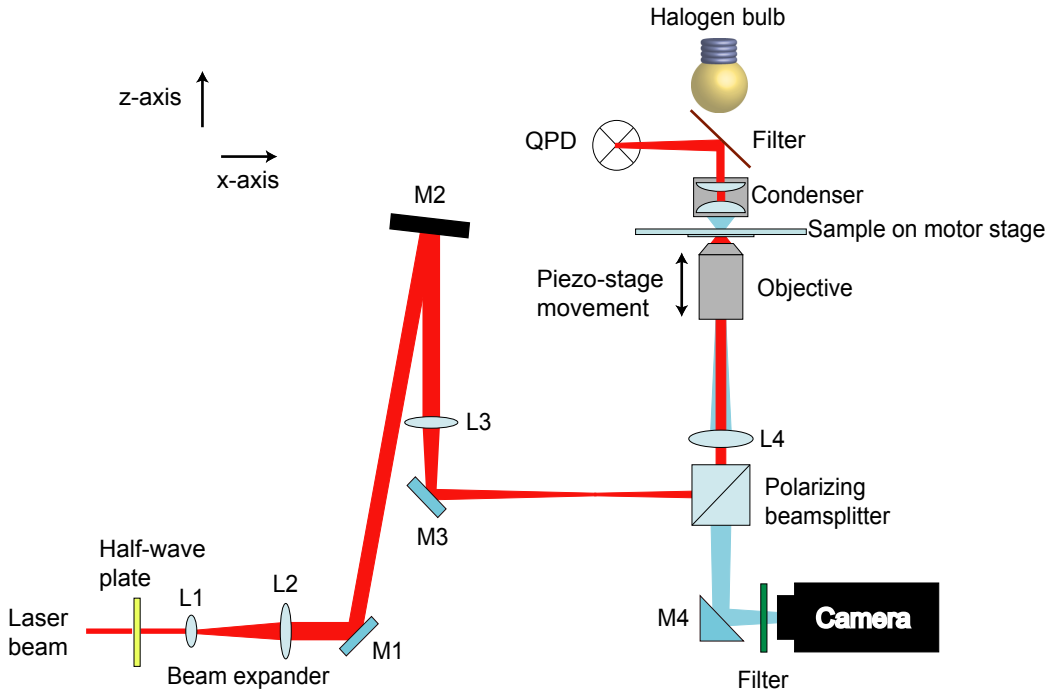

Figure 2.2: Typical holographic optical tweezers setup. Lenses L1 and L2 form the beam expander, and lenses L3 and L4 form the telescope after the beam-steering mirror, M2. Lens L4 also images the sample onto the camera. The half-wave plate orients the polarization of the laser beam with the polarizing beam-splitter. The quadrant photodiode is in the back-focal plane of the condenser lens and can be used to track the particle position.

2.3 Measuring Particle Position

In many biological applications of optical tweezers, transparent beads are attached to the biomaterial under study, thus acting as 'handles' that can be used to measure or apply forces. To enable trap calibration and subsequent force measurements, the particle position must be determined to a high enough accuracy and at a bandwidth of at least tens of Hz (depending on the trap strength). Although the sample is often imaged onto a standard video camera for visualisation, the particle tracking is often carried out using a quadrant photodiode (QPD) in the back-focal plane of the condenser lens

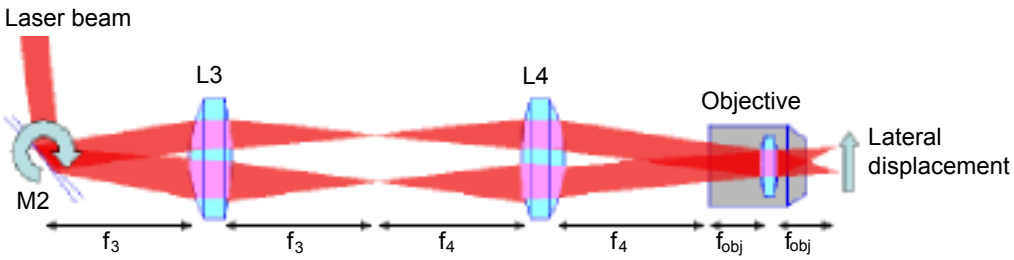

Figure 2.3: The laser light is directed through a microscope objective using a beam steering mirror (M2) and telescope arrangement with 4f-imaging (L3 and L4) to allow angular deviations of the beam to cause lateral translation of the trap in the trapping plane. Courtesy of Molloy and Padgett [21]

[22, 23, 24, 25, 26, 27], shown in figure 2.2. QPDs are the common choice for measuring forces since they offer high-bandwidth measurements, typically several kHz, whereas standard video cameras are limited by acquisition rates of only 10s of Hz. Standard video frame rates are therefore often too slow compared to the decay time (damped harmonic motion) of a typical trap.

2.4 Trap calibration

A trapped colloidal particle is localised to within approximately a particle radius of the trap center, depending on the trap strength. The trap suppresses low frequency motion of the particle but the particle still exhibits residual Brownian motion at higher frequencies. For small displacements of the particle from the centre of the trap, the motion of a trapped particle is that of a thermally excited, over-damped oscillator in a harmonic potential. Figure 2.4 shows an example of the residual Brownian motion of a particle in optical tweezers. The particle's Brownian motion is restricted to the confines of the trap.

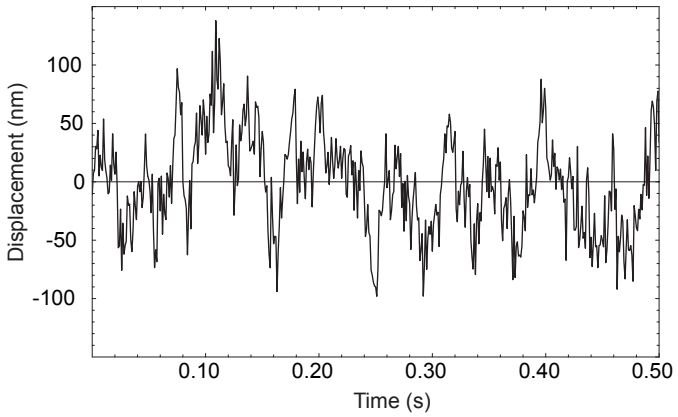

Figure 2.4: Experimental data taken of the positional fluctuations of a 2μm silica particle trapped with optical tweezers in water.

The trap can be treated as a Hookean spring and characterized by a spring stiffness, κ [21, 28]. The trapping force f_{trap} exerted on the particle by the trap is $f_{trap} = -\kappa x$, in one dimension, where x represents the position with respect to the trap center. By calibrating the trap strength, it is possible to measure the force exerted on the trapped particle by measuring it's displacement from the centre of the trap. The trap strength is directly proportional to the laser power, so by increasing the power in the trap the particle exhibits a decrease in the variance of positional fluctuations.

The trap strength can be estimated by modelling the trap, using knowledge of the laser power in the trap, the particle size and optical properties of the particle and fluid. However, in many cases these factors are not known to sufficient accuracy. This is often the case with biological samples, where the refractive index may even be changing over time. To allow quantitative measurements to be made, trap calibration is often determined experimentally.

Stokes drag force

On micron length scales, in liquid media, the Reynolds Number is very small, meaning that the forces arising from the viscosity of the fluid are dominant over its inertia. In the case of colloidal particles in water the Reynolds number is approximately in the range 10^{-9} to 10^{-4} so an approximation of the Navier-Stokes equation for incompressible fluids can be used, called the Stokes equation:

$$\eta \nabla^2 \mathbf{u} = \nabla \mathbf{p}, \tag{2.2}$$

where η is the fluid's viscosity, $\mathbf{p}$ is the local pressure and $\mathbf{u}$ is the fluid velocity. On the abscence of sources or sinks [29]:

$$\nabla . \mathbf{u} = 0. \tag{2.3}$$

Stokes found the force, f, needed to translate a sphere of radius a through an unbounded, viscous, quiescent fluid of viscosity η at a constant velocity ν to be

$$f = \gamma_0 \nu, \tag{2.4}$$

where the viscous drag coefficient,γ_0, for a sphere in an unbounded fluid is:

$$\gamma_0 = 6\pi\eta a. \tag{2.5}$$

where η is the viscosity and a is the radius of the sphere.

The drag coefficient for a spherical particle can be calculated from the above equation if the particle size is known, provided it is far from surfaces, in a fluid of known viscosity. A constant external force can be applied to a trapped spherical particle by moving it through the damping fluid with a known constant velocity or by moving the fluid past the particle with the

trap static. In practise it is easier to keep the trap position static and move the fluid past the trapped particle by moving the sample with the motorized stage or by using a microfluidic setup.

The particle position can be measured by analysing the video images from a standard camera with particle tracking software. As long as the particle remains trapped, the Stokes drag force will be equal to the trapping force so the trap strength, κ, can be calculated using the relation

$$6\pi\eta a\nu = \kappa x. \tag{2.6}$$

Thermal analysis

Alternatively, analysis of the residual Brownian motion of the trap can determine the trap stiffness and fluid properties without the need for stage movement.

From the equipartition theorem, the energy in the Brownian motion of the trapped bead in one dimension is equal to $\frac{1}{2}k_BT$. Treating the trap as a Hookean spring, the energy is equal to $\frac{1}{2}\kappa\langle x^2\rangle$. So the trap stiffness is given by

$$\kappa = \frac{k_BT}{\langle x^2\rangle} \tag{2.7}$$

The trap stiffness is simply calculated by measuring the variance of the particle's positional fluctuations in a fluid at a known temperature. Positional measurements need to be taken for longer than the characteristic decay time of the trap, which in practise is of the order of milliseconds. This method has the advantage of fast computation and does not require knowledge of the fluid viscosity. However, the variance is particularly susceptible to any drift or low frequency noise in the positional data (perhaps caused by laser pointing stability or mechanical vibration). For this reason

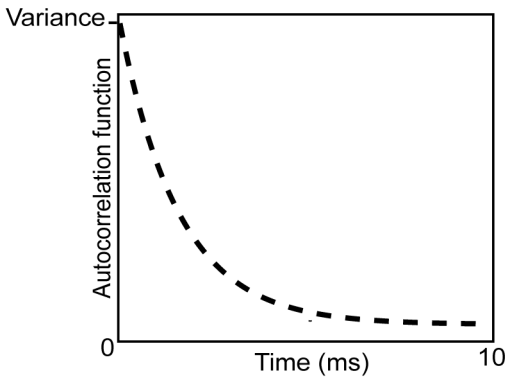

Figure 2.5: Illustration of the position autocorrelation function of a particle in a trap.

it can be useful to limit the time window; this is discussed in more detail later in this chapter.

Another thermal analysis method involves modelling the motion of a particle in an optical trap with the Langevin equation [30], which in one dimension is:

$$m\ddot{x}(t) + \gamma_0\dot{x}(t) + \kappa x(t) = F^B(t), \tag{2.8}$$

where $x(t)$ is the position relative to the center of the trap, m the mass, and $F^B(t)$ represents the Brownian forces acting on the particle. For an underdamped system the autocorrelation function would show an oscillation with exponentially decreasing amplitude, this is covered in more detail in Chapter 7. In optical tweezers experiments in water the inertial term can be dropped as the system is heavily overdamped. This can be solved for $x(t)$ to find the autocorrelation function $\langle x(t)x(0)\rangle$ of the particle's position in one dimension to be:

$$\langle x(t)x(0)\rangle = \frac{k_BT}{\kappa} exp(-\frac{\kappa}{\gamma_0}t). \tag{2.9}$$

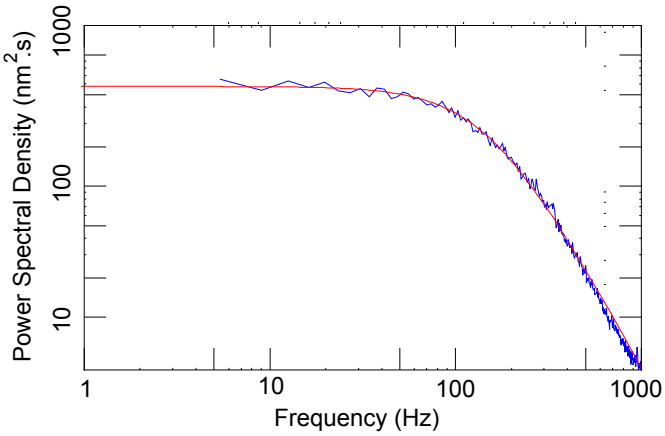

Figure 2.6: Experimental data from a 2μm silica bead in optical tweezers in water. The power spectral density is plotted against frequency, each point represents the mean of 300 points.

The position autocorrelation function decays exponentially to zero with a decay-time, $\tau = \gamma_0/\kappa$, (see Figure 2.5). This intercept and decay time can be found by fitting an exponential to the autocorrelation function. At the intercept, $t = 0$, the position autocorrelation function is equal to the variance of the positional fluctuations, so the trap strength is given by Equation 2.7. The drag coeffcient can then be calculated using the trap strength and decay time. If the radius of the particle is known then the viscosity can also be calculated from the drag coefficient [31]

$$\eta = \frac{\tau k_B T}{6\pi a \langle x^2 \rangle}. \tag{2.10}$$

Alternatively, in the frequency domain, power spectrum analysis can be used, as explained by Berg-Sörensen *et al.* [28]. The power spectral density $S_x(f)$ of the x-axis positional data is approximately a Lorentzian of the form:

$$S_x(f) = \frac{k_B T}{2\pi^2 \gamma_0 (f^2 + f_c^2)} \tag{2.11}$$

where f is the frequency and $f_c = \kappa/2\pi\gamma_0$ is the corner frequency. The length of the time period over which the power spectral density is calculated

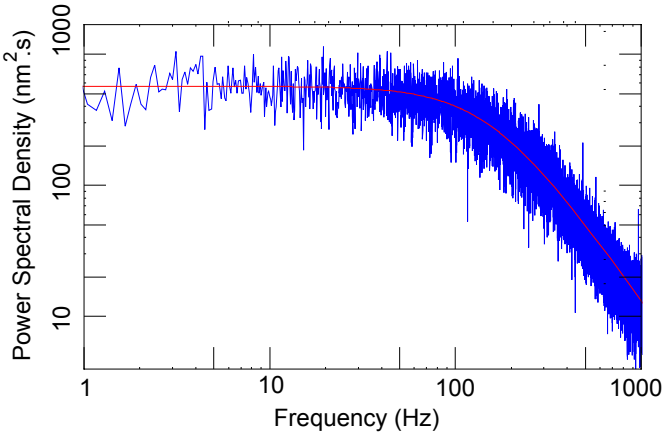

Figure 2.7: The same experimental data as figure 2.6. Power spectral density plotted against frequency, each point represents the mean of 10 points.

should be much larger than the cut-off frequency to ensure enough low frequency data points to fit to. Least squares-fitting of the data points to a Lorentzian requires that the points are Gaussian-distributed about the mean for statistical correctness. In this case, however, the points in the power spectrum are exponentially distributed about the theoretical limit so Berg-Sörenson *et al.* recommends 'blocking' [28] the data to remedy this before fitting. A 'block' of consecutive data points of the power spectrum is replaced with one point at the mean frequency and mean S_x. Figure 2.7 shows the power spectral density (with Lorentzian fit) for a trapped 2μm diameter particle, with points blocked into blocks of ten. Figure 2.6 shows the same data blocked in blocks of 300. Tolić Nørrelykke *et al.* suggests at least 100 points per block and at least 50 blocked points for fitting the Lorentzian [32]. By blocking together a large enough number of points the blocked data is to a good approximation, Gaussian-distributed so least-squares fitting can be applied.

Although otical tweezers are often mounted on air damped optical tables, and optical components are mounted close to the table to reduce effects of mechanical resonance on position measurements, noise can still be an issue. For all thermal analysis methods the positional data can be affected by

drift in the system so it can be wise to consider the Allan variance [33] of the positional data first to indicate the timescale over which the system is dominated by Gaussian noise or drift. The Brownian motion is a Gaussian process and the mean position should tend to zero at large times as the fluctuations average out. When averaged over multiple measurements, the standard error of the average position of the trapped particle is dependent upon $\langle x^2 \rangle$ and the number of independent measurements, N. In a time Δt, the number of independent measurements is given by

$$N \approx \frac{\Delta t}{\sqrt{2}\tau_0} = \frac{\kappa \Delta t}{\sqrt{2}\gamma} \tag{2.12}$$

giving the standard error of the particle position, $SE_{\langle x \rangle}$, to be

$$SE_{\langle x \rangle} = \sqrt{\frac{\langle x^2 \rangle}{N}} \approx \sqrt{\frac{\sqrt{2} k_B T \gamma}{\kappa^2 \Delta t}}. \tag{2.13}$$

Averaging the data over longer time-windows improves the accuracy of the measured mean position and variance in proportion to the square root of the number of measurements. However, at longer timescales the drift (systematic error) becomes greater than any improvements in the accuracy of the mean position or variance. This transition between the two regimes indicates the useful time over which the system can be said to be stable and can help decide on the time-window to use when calibrating a trap. The Allan variance of position given by

$$\sigma_x^2(\tau) = \frac{1}{2} \langle (x_{n+1} - x_n)^2 \rangle \tag{2.14}$$

where x_n is the average position over the sample period n, and τ is the time per sample period.

At timescales above the autocorrelation decay time, the bead positions are randomly distributed within the trap and the accuracy of the mean is proportional to the square root of the averaging time. After 50 seconds, the Allan variance increases, which is a result of drift within the system. One

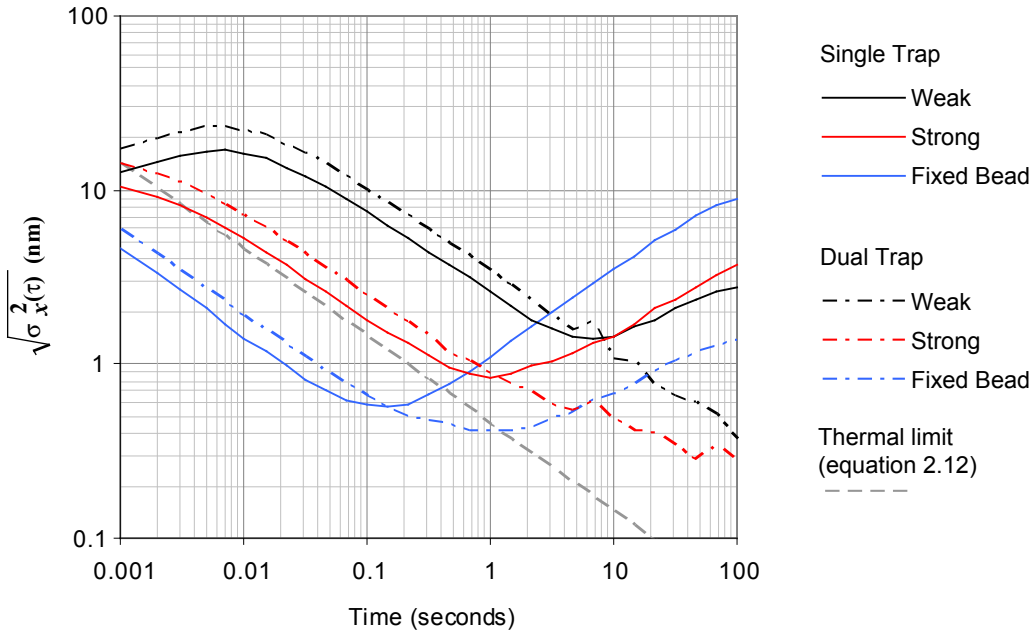

Figure 2.8: Experimental data showing stability of position measurements by plotting Allan variance against time. The blue lines correspond to the single and differential measurements of two 2μm silica beads that were fixed to the microscope coverglass, having a separation comparable to the trapped beads. The thermal limit is estimated for the strongly trapped bead. Weak trap (7mW, κ = 5.6x10^{-6} N/m), strong trap (37mW, κ = 2.3x10^{-5} N/m). Data and graph courtesy of Gibson [34].

method of gaining longer term stability of the system is to take measurements of the differential position of two trapped particles. Most of the unwanted noise in the system similarly affects both trapped particles, so by tracking the differential position much of it can be removed from data, as shown in Figure 2.8.

Longer term stability is realised at the expense of a $\sqrt{2}$ increase in noise since the Brownian motion of the two beads add in quadrature. Shown also in Figure 2.8 is the Allan variance of the position measurement of beads fixed to the coverslip. At short timescales the Allan variance is limited by noise from the camera, but at longer timescales it increases above that of the trapped bead. This increase at long timescales indicates that the

thermal, or other, stability of the sample stage is worse than the pointing stability of the laser.

In practise, when collecting data for calculating the variance, autocorrelation function or power spectrum, the analysis can be simplified by using a time window much shorter than the time at which external noise limits its measurement accuracy. In our setup the for the case of a single bead measurement, the optimum averaging time is in the range of 1-10 seconds. Also, increasing the trap power results in a higher measurement precision.

2.5 Holographic Optical Tweezers

To allow multiple traps in the sample plane the laser beam can be either split up into multiple beams or alternatively the beam can be rapidly scanned between multiple trap positions. A time sharing technique can effectively trap tens of particles if the laser beam is scanned much faster than the time it takes for one of the particles to diffuse away from the trap. Two common time sharing techniques use scanning mirrors [35] or acousto-optic modulators [36].

Instead of using the time sharing techniques the light can be split up by a diffractive optical element in the Fourier plane of the sample. Originally this was achieved using a microfabricated plate, designed and prepared in advance [37], which created patterns of stationary traps in a 3D volume.

In the late 90s, optical tweezers were revolutionised by the incorporation of spatial light modulators (SLMs) [38] in the Fourier plane of the sample. An SLM is a computer controlled diffractive optical element that can be used to adjust the phase of the reflected light. The SLMs used for optical tweezers applications are commonly based on nematic liquid crystals. The front of the SLM consists of a pixellated display, where each pixel modulates the phase of an incident light beam [39, 40]. The phase-pattern displayed

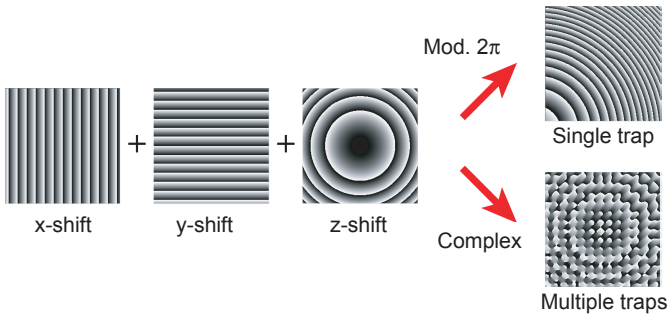

Figure 2.9: An example of kinoform addition for x,y,z shifts for a single trap and multiple traps.

on the SLM is called a kinoform and can be calculated in such a way as to give an angular displacement of the diffracted beam and hence a lateral displacement of the trap in a similar way as achieved with the beam-steering mirror in figure 2.3 [41]. Thanks to this new technology, independent positional control, including axial displacement, of multiple optical traps in a 3D volume could be realised [42, 43, 44].

An example of a some simple kinoforms are shown in figure 2.9. The shades of grey represent the phase level of the pixels (0 to 2π) across a pixellated SLM. With more complex kinoforms, a single laser beam could be divided to form many discrete traps. It is also possible to use an SLM to create beams possessing orbital angular momentum, one such beam is called a Laguerre-Gaussian beam [45], which are discussed further in Chapter 3.

Holographic optical tweezers enable the trapping and manipulation of tens of particles in "real time", with kinoforms being updated interactively using a PC. The number of traps is limited by the laser power available and eventually by the maximum laser power permitted to be incident on the SLM (to avoid overheating). Calculating the required kinoform to be displayed on the SLM to achieve the required pattern of traps in 3 dimensions can be processor intensive. Many algorithms can be used to calculate the kinoforms, some being particularly fast, appropriate for interactive uses [46]. When higher control of trap intensity is required, other, slower algorithms

can be used to pre-calculate the kinoform [47]. Generally, the more time-consuming the kinoform calculation, the more efficient the kinoform will be at directing light into the trap. Some light is always lost into ghost orders, even with a supposedly perfect kinoform, as a consequence of the pixellation and other imperfections of the SLM display.

SLMs are now routinely used for dynamic control of multi-particle arrays in 2 [37] and 3 dimensions [39, 48, 49, 42]. The kinoform to be displayed on the SLM can be calculated and displayed typically faster than a few Hertz depending on the number of traps. The problem of calculating kinoforms can be implementing parallel calculations, utilising the multiple processor cores of many PCs. This can be vastly improved if hologram calculation is carried out using a graphics card, effectively using many parallel processes rather than a typical central processor unit (CPU) [41].

CHAPTER 3

Direct measurement of the skew angle of the Poynting vector in a helically phased beam

3.1 Introduction

This chapter presents the use of a "'smart camera"' with integrated particle tracking built by Durham Smart Imaging and is based on published work [16]. The experiment was carried out at Durham University by myself, Jonathan Leach, Chris Saunter and Gordon Love. A spatial light modulator and Shack-Hartmann lenslet array [50] are used to determine the local skew angle and direction of the Poynting vector l within a helically-phased beam. Rapid, simple and non-ambiguous determination of the sign of l and azimuthal direction of the momentum is particularly important in optical tweezing experiments [51] especially those involving the transfer of light's angular momentum [52]. Measurement of orbital angular momentum in this

way is an alternative to interferometric techniques giving a non-ambiguous result to both the magnitude and sign of l from a single measurement, without any restriction on the optical bandwidth or coherence length of the laser.

Although not using optical tweezers, the experiment demonstrates the ability of the "Smart Camera" to track a large number of particles without data management problems. This highlighted the possibility of using such a camera in optical tweezers for high-speed tracking of multiple particles. Further development of the camera allowed subsequent use in experiments with optical tweezers.

Beams with helical phase fronts, characterized by an azimuthal phase term $exp(il\phi)$, possess an orbital angular momentum of $l\hbar$ per photon [53, 54], where ϕ is the azimuthal angle and l is an integer. Unlike spin angular momentum that is linked to circular polarization, and ultimately to the photon spin, the orbital angular momentum is solely a function of the form of the optical phase front. This azimuthal phase structure can be studied with an interferometer, where the azimuthal phase term results in the characteristic spiral interference pattern with l radial fringes [55]. The l-fold rotational symmetry can also be utilized within a Mach Zhender interferometer to sort an input beam between two or more outputs depending on the value of l [42]. Interferometry requires sub-wavelength experimental precision and eliminating the ambiguity associated with the sign of the gradient of the wavefront strictly requires multiple interferograms and phase stepping techniques. This ambiguity is particularly pertinent to beams with a helical phase since the number of fringes depends only upon the modulus of the orbital angular momentum l . Determining the sign of the orbital angular momentum, clockwise $+ve$ l or anticlockwise -ve l requires further measurements.

The Poynting vector in helically phased beams

Within the paraxial approximation, any linearly polarized, helically-phased beam of complex amplitude $u(r, \phi, z) = u(r, z)exp(il\phi)$, of which Laguerre-Gaussian and high order Bessel beams are both examples, has r -, ϕ - and z -components of linear momentum density, $\mathbf{p} = \epsilon_0 \mathbf{E} \times \mathbf{B}$, given by [53]

$$p_r = \varepsilon_0 \frac{\omega k r z}{(z_R^2 + z^2)} |u|^2, \; p_\phi = \varepsilon_0 \left[\frac{\omega l}{r} |u|^2 \right] and \; p_z = \varepsilon_0 \omega k |u|^2. \tag{3.1}$$

where $\mathbf{E}$ and $\mathbf{B}$ are the electric and magnetic field strengths respectively, ω and k are the angular frequency and the wavenumber of the light and z_R is the Rayleigh range of the Gaussian beam. ϵ_0 is the dielectric permittivity. For a well-collimated beam, $p_r \approx 0$, and p_ϕ / p_z gives the skew angle, γ , of the Poynting vector with respect to the beam axis to be $\gamma = l/kr$ [56, 57]. An illustration of a Laguerre-Gaussian beam is shown in Figure 3.1. For $l = 1$, $\lambda = 632$ nm and $r = 1mm$, γ is only 0.1 milliradians. Resolving the linear momentum of the photon k, into its corresponding azimuthal and axial components and multiplying by the radius, r, is compatible with the orbital angular momentum around the beam axis being l per photon. The skew angle of the Poynting vector gives rise to an azimuthal shift of the beam behind a linear obstruction [58] and/or a shift in the interference pattern produced by Young's double slits [59]. However, rather than relying on these subtle effects or inverting potentially ambiguous interferometric data, the Shack Hartmann wavefront sensor can be used to measure the skew angle of the Poynting vector directly.

Generation of helically phased beams and the Shack Hartmann wavefront sensor

The helically phased beams investigated in this study were generated using a HoloEye Photonics AG SLM, configured as a diffractive optical element. When programmed with an $l-$forked diffraction grating [60], the

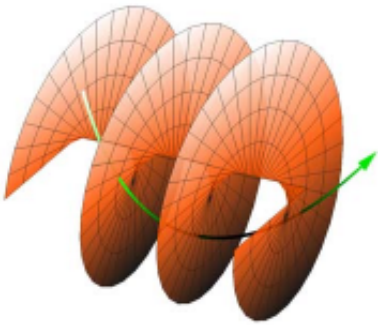

Figure 3.1: A diagram showing a surface of constant phase around an optical vortex with the Poynting vector indicated by a green line. Figure courtesy of O'Holleran [1]

first-order diffracted beam has helical phase fronts described by $exp(il\phi)$. The Laguerre-Gaussian (LG) modes are a convenient basis set from which to describe beams with helical phase fronts, and are given by [61]

$$u_{pl}^{LG} = \frac{C_{pl}^{LG}}{w(z)} \left(\frac{r\sqrt{2}}{w(z)} \right)^{|l|} exp\left(-\frac{r^2}{w^2(z)} \right) L_p^{|l|} exp\left(-\frac{ikr^2 z}{2(z^2 + z_R^2)} \right) \tag{3.2}$$

$$exp(-il\phi) exp\left(i(2p + |l| + 1) tan^{-1} \frac{z}{z_R} \right), \tag{3.3}$$

where C_{pl}^{LG} is the normalisation constant; $L_p^{|l|}$ is a generalised Laguerre polynomial; w(z) is the radius of the beam at position z, where $w(z)^2 = \frac{2}{k}\frac{z_R^2 + z^2}{z_R}$; $(2p + |l| + 1)tan^{-1}\frac{z}{z_R}$ is the Gouy phase. p and l are mode indices, where l corresponds to the azimuthal phase terms and p is the number of radial nodes.

A Shack-Hartmann wavefront sensor employs a micro-lens array to generate a matrix of spots on an imaging array. Any local inclination of the incident wavefront causes a lateral displacement of the corresponding spot [62, 50]. For this work we use lenses with a 70mm focal length arranged on a square array with a pitch of 300μm. A local wavefront inclination of 0.1 milliradians gives a displacement of the focused spot by 7 microns, comparable to the spot diameter. The camera can determine the relative spot position to 700nm giving a precision for measuring the local direction of

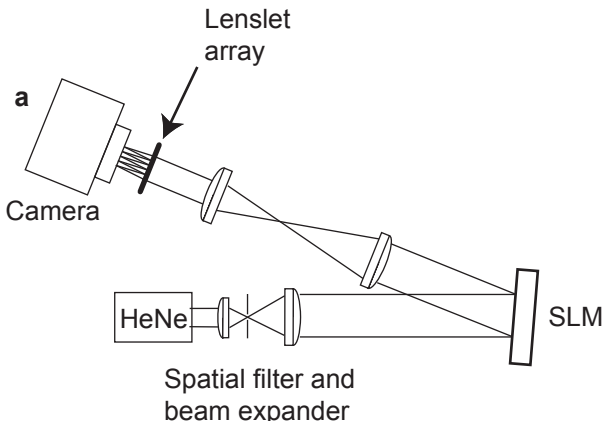

Figure 3.2: (a) Experimental setup for measuring the local inclination of the Poynting vector.

the Poynting vector of 0.01 milliradians. Figure 3.2 shows the experimental arrangement of the HeNe laser, beam expander to ensure illumination of the SLM aperture, and the Shack Hartmann wavefront sensor. A 4f imaging system (where f is the focal length of one of the lenses) was used to image the plane of the SLM and control the size of the beam incident on the lenslet array. In order to generate pure LG beams, it was necessary to control both the intensity and the phase of the incident light. This was achieved by adjusting the local contrast on the SLM to shape the intensity of the light beam accordingly [63, 42]. Figure 3.3(a) shows how an LG beam is created using a spiral phase plate with Figure 3.3(b) showing an example of a kinoform used to create an LG beam.

Results and Discussion

Figure 3.4 shows a series of vector fields illustrating the measured skew angle of the Poynting vector for LG modes with l values ranging between +5 and -5. The length and direction of each vector arrow corresponds to the movement of the spot produced by a single lenslet within the Shack Hartman array. Where the intensity was too low to make an accurate measurement of the spot position, the arrow has been omitted. Figure

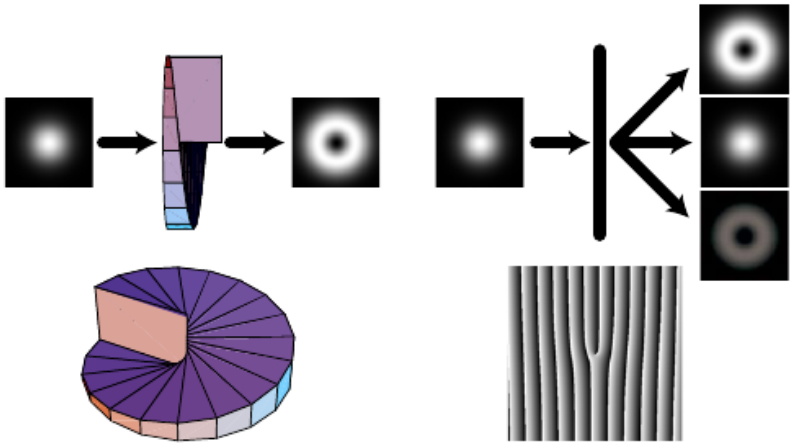

Figure 3.3: Illustration of a Gaussian beam incident on (a) a spiral phase plate of height $\lambda\theta/2\pi$ and (b) a hologram with phase modulation $mod2\pi|\lambda\theta/2\pi + \alpha x|$ where the second term adds a blazed diffraction grating, to preferentially diffract light into the positive first order. Figure courtesy of O'Holleran [1]

3.5 is a graph derived from the same data as displayed in 3.4 showing the relationship between the measured skew angle of the Poynting vector, the beam radius and the azimuthal mode index. As anticipated, there is a close agreement between these measurements and the predicted value of $\gamma = lkr$.

The technique can also be used to measure the l value of a Laguerre-Gaussian mode. For each lenslet within the array, the expression for the skew angle of the Poynting vector can be rearranged to give $l = \gamma kr$. The value of γkr can then be averaged over all the lenslets to give a measure of l and hence the orbital angular momentum per photon, see Figure 3.6. Note that the error in the mean value is typically <0.1, demonstrating that a Shack-Hartmann lenslet array can be used as an unambiguous method for measuring the orbital angular momentum per photon of LG beams.

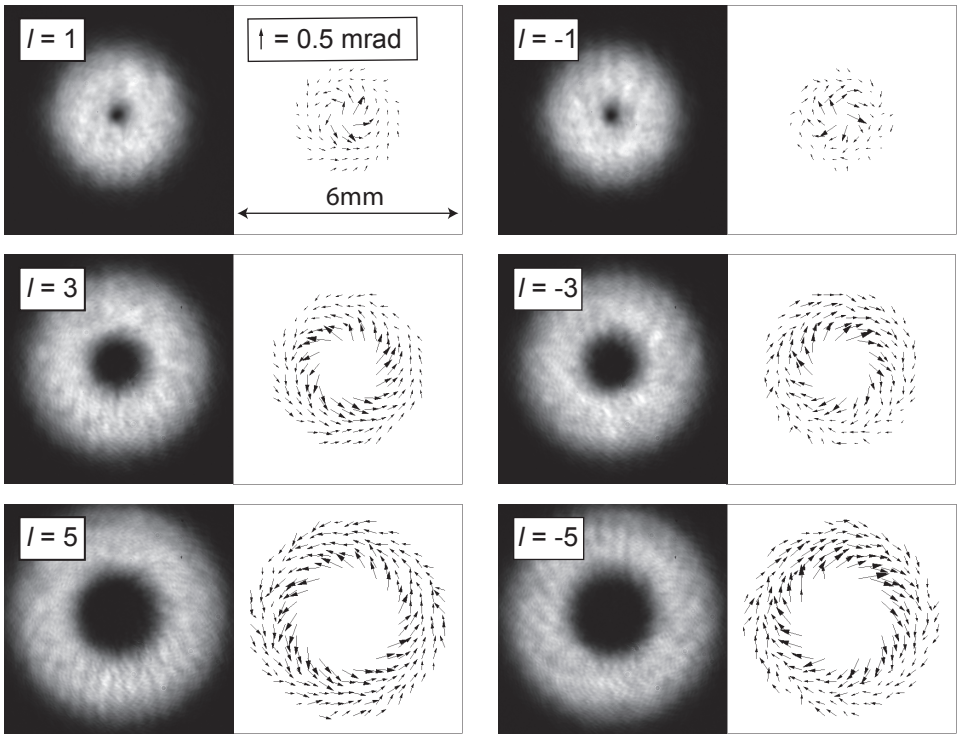

Figure 3.4: Intensity and vector plots showing the measured inclination of the Poynting vector for different values of l. Both positive and negative values of l are shown. Courtesy of Leach [16].

Conclusions

We have shown that the local skew angle of the Poynting vector within a helically-phased, $exp(il\phi)$, beam can be measured using a Shack Hartmann wavefront sensor. We have confirmed that this skew angle is in close agreement with that expected, corresponding to an orbital angular momentum of l per photon. Beyond a simple confirmation of the structure of helically phased modes, the technique is particularly suited for making unambiguous measurements of the sense of the orbital angular momentum in experiments based on momentum transfer. This non-interferometric technique requires only a single, exposure and is hence ideally suited to use with pulsed or white light sources. It is also applicable to the analysis of more complex modal superpositions with differing values of l , such as elliptical [64] or

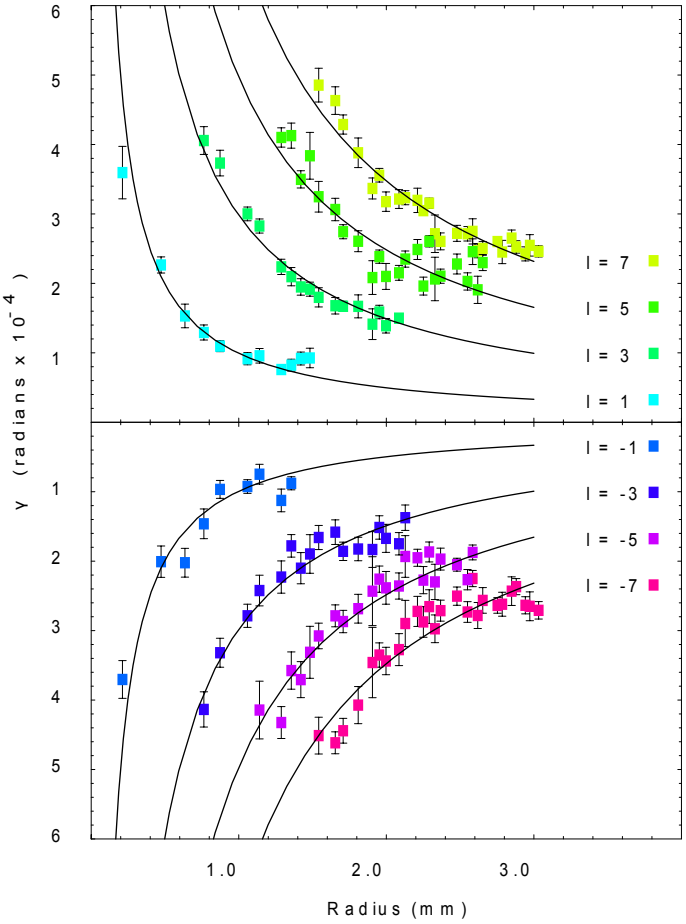

Figure 3.5: The relationship between the measured skew angle of the Poynting vector, the beam radius and azimuthal mode index, l; in close agreement with the predicted value, $\gamma = l/kr$. Courtesy of Leach [16].

spiral [65] beams that, although possessing orbital angular momentum, do not have a single value of l .

The valuable feature of the "smart camera" is its ability to track particle positions at high-speed and save the positional data in real-time without images and so, therefore effectively prevents data management problems. A decision was made with our collaborators at Durham University for them to modify the camera to allow its use for tracking in optical tweezers. While modifications were carried out an experiment was undertaken using a commerical CCD high-speed camera in optical tweezers, which is presented in

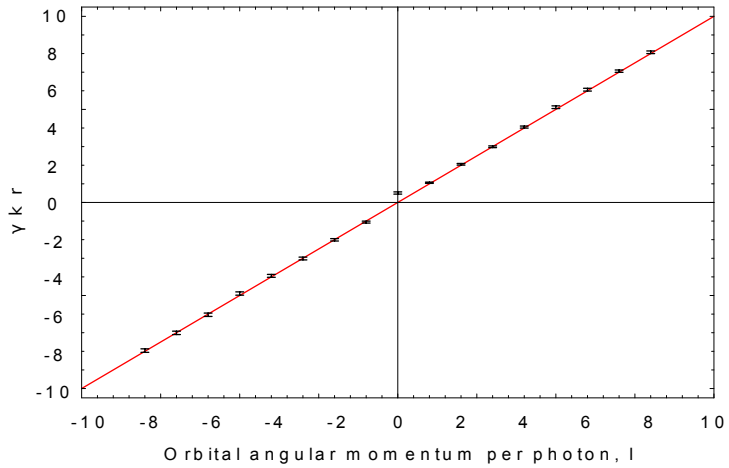

Figure 3.6: The mean value of $\gamma\ kr$ calculated from the data in 3.5. The error bars show the error in the mean value. Courtesy of Leach [16].

the next chapter.

CHAPTER 4

Measuring particle position

4.1 Introduction

This chapter presents a demonstration of the feasibility of using a high-speed CCD camera to measure particle positions by collecting positional data from the camera and a QPD simultaneously. This experiment was carried out primarily by myself with help and advice from Jonathan Leach and Graham Gibson.

Particle tracking with a QPD

A QPD consists of 4 light-sensitive quadrants each with an independent output to an amplifier. The QPD can be positioned in the imaging plane of the sample (same plane as the video camera), or alternatively it can be placed in the back-focal plane of the condenser lens, where an interference pattern can be tracked [22]. This QPD arrangement can measure the centre-of-mass of the particle to within less than 10nm at tens of kHz.

A QPD placed in the back-focal plane of the condenser, as explained in [22], can be used to track the particle position relative to the trap center. The particle does need to be homogenous and spherical though, so a biological particle could not easily be used. Instead, it is common for silica or polystyrene microspheres (attached to biological material of interest), to be tracked. The interference pattern is projected onto the QPD. The signal from the amplifiers is relayed to a National Instruments data aquisition card. If the QPD is initially centered with the interference pattern then deviations in the position of the interference pattern of the four quadrants will indicate particle position fluctuations within the imaging plane. The signals from the individual quadrants are divided by the total signal so as to correct for any intensity variations in the signal. Effectively, the QPD measures the center-of-mass of the particle. Calibrating the signal from the QPD in terms of nm per volt is critical. Commonly the position of a stuck particle on the coverslip is tracked while the motor stage (holding the coverslip) is moved back and forth over fixed distances. This method does unfortunately introduce some error as the calibration factor can vary depending on the position of the tracked particle in the $z - axis$ (the laser propagation axis). So the correct calibration factor may be different for a trapped particle 10 μm from the coverslip as opposed to one that is stuck to the coverslip. Alternatively, a QPD system can be calibrated at the height above the coverslip they intend to take measurements, by displacing the bead known distances from the trap center using the drag-force method. However, this method requires knowledge of the drag coefficient and trap stiffness. Although the trap stiffness can be calculated accurately by power spectral analysis with an uncalibrated QPD, knowledge of the drag coefficient is limited by particle size uncertainty and unknown fluid viscosity. Generally the voltage signal is found to be linearly related to the displacement of the particle for displacements of less than a particle diameter [66]. A variation of this method is to use a second laser solely for tracking instead of using the trapping laser. The advantage being that multiple particles can be tracked with the trapping laser and the tracking laser is independent so it can be moved to track the position of any of the particles in turn. However,

it is difficult to track many particles simultaneously using a QPD arrangement. Two particles have been tracked using two QPDs before [25] but to extend this technique to more particles would be cumbersome.

Video Particle Tracking

Video particle tracking is appropriate when determining the trap strength through the Stokes drag-force method but usually the frame rate is too low for calculating the trap stiffness in a typical trap by thermal analysis of the particle. However, video cameras are convenient to use and allow multiple particles to be tracked simultaneously over large fields of view. However, recording the images from a standard video camera for many minutes, which may be required, can be a challenge in data management. Particle tracking software can be used to analyse the recorded images of the trapped particle from a standard video camera. Video particle tracking has been shown to achieve positional accuracy of less than $10nm$ (sub-pixel accuracy) at a frame rate of approximately 30 Hz [67, 68]. The positional accuracy is not limited by the wavelength and has no obvious theoretical limitation, unlike the optical resolution.

The accuracy at which a particle can be tracked depends on the tracking algorithm used, the microscopy details, and noise in the system. If the particles are imaged slightly out of focus onto the camera sensor, a parabolic fit tracking method can be used. The pixels are summed in the x and y axess within a user-defined region of interest around the image of the trapped particle. The summed intensity in x and y each fit a parabolic fit to the intensity. This has the advantage of being computationally simple so a fast way of tracking particle position. Another, more accurate method involves using a template image and finding the correlation between the template and images of the particle. However, this method is computationally expensive so limiting the ease of use for large amounts if images. This is discussed further in a recent practical review of particle tracking *et al* [68].

The image size compared to the camera pixel size affects the tracking accuracy. If the optical magnification of the microscope is decreased the image size will decrease so the particle will be represented by fewer pixels. This results in a linear loss of accuracy with lower magnification if the signal to noise is unaltered. However, the illumination decreases as magnification increases so reducing the signal to noise (S/N). The reduction in S/N puts a practical limit on magnification of around 30-40nm/pixel according to Carter *et al* [68]. Carter also concludes that NA has very little effect on accuracy unless you have low S/N in which case increasing NA increases accuracy. In an optical tweezer setup, a high NA (1.3) microscope objective is already in use so improvement is unlikely with regards to NA.

An alternative to using a QPD or standard video camera is a high-speed video camera that can record images at several kHz for particle tracking software to analyze. However, high-speed video cameras are not themselves without limitations, bright illumination is needed and data management is an important issue. CMOS cameras can achieve frame rates of the order 1kHz with reduced field of view (horizontal and vertical), and the data can be managed in real time using a standard desktop PC[69].

4.2 Experimental Setup

The optical tweezers setup including high-speed camera is shown in Figure 4.1. A 2W 1064nm continuous wave laser was used for trapping. The x100, 1.3 NA. microscope objective was used to focus the laser light to form an optical trap approximately $100\mu m$ from the objective. A halogen 100W light bulb and 0.8 NA condenser illuminated the sample with a Köehler illumination arrangement. The objective and tube lens imaged the sample onto a Motionscope M2 CCD high speed camera mounted to the viewing port of the microscope. The QPD particle tracking was carried out using a separate low power helium-neon (HeNe) laser with a New Focus QPD in the

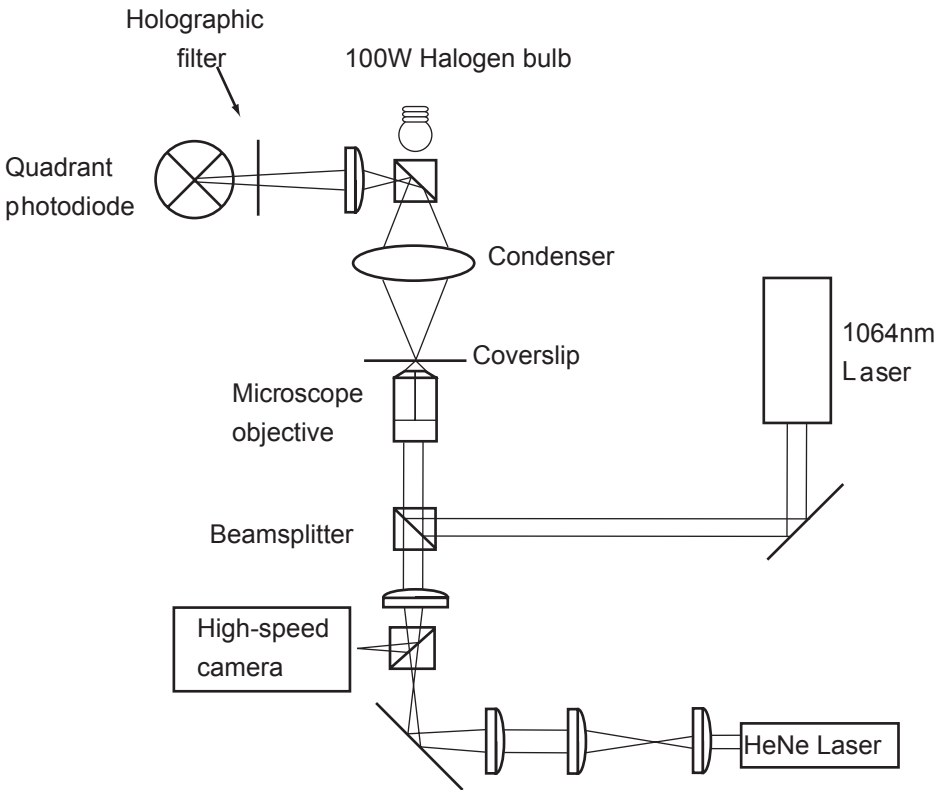

Figure 4.1: Experimental setup for measuring particle position in optical tweezers using a quadrant photodiode—with separate tracking laser—and a high-speed video camera mounted to the viewing port of the microscope.

back-focal-plane of the condenser [70, 8]. The HeNe was aligned with the trapping beam using a beam-splitter before passing through the objective. The HeNe light transmitted through and around the trapped particle passed through the condenser to the QPD, which had a holographic filter attached to prevent the trapping laser light from reaching the QPD. The differential output from the QPD was amplified before being logged by a National Instruments data acquisition card.

The camera can record video at a range of different frame rates but to reach the higher frame rates the number of rows read on the CCD sensor needs to be reduced, which in practise restricts the field-of-view of the camera. Our illumination was of sufficient brightness that a frame rate of 2kHz and a

resolution of 1024x256 gave high quality images. The 2Gb of buffer memory within our camera meant that we could record 4 seconds of data, after which the images were transferred by firewire to a computer hard drive. Although the QPD has a higher bandwidth, for this comparison it was set to the same speed as the camera (2kHz).

A piezo-stage was used to displace a fixed particle (stuck to the coverslip) a known distance, calibrating the camera in terms of nanometers per pixel and the QPD in terms of nanometers per volt.

Samples consisted of silica microspheres dispersed in water at low concentration, the mixture was agitated in an ultrasonic bath briefly to reduce the chances of spheres sticking together. The fluid is then dropped by pipette into a well in a standard glass-slide. A coverglass is placed on top with care so as to avoid bubbles being trapped in the sample. Excess fluid is gently pressed out from between the coverglass and coverslip and then glue is used to permanently seal the sample to avoid any evaporation, which can cause fluid flow during an experimental run.

The particles were imaged slightly out of focus onto the camera sensor so that the particles appear as a bright circle with a parabolic intensity profile encircled by a dark ring. This allowed the employment of a parabolic-fit tracking algorithm to be used on the saved images. The tracking program was written in LabVIEW, the images were displayed in the program for the user to define a close-fitting region of interest around the particle. Another method, which does not necessarily require the particle to be imaged out of focus, is an edge detection algorithm. The 'find circle edge' built-in function in Labview can be used. However, it was found to give similar results but was slower and more care had to be taken adjusting parameters beforehand to ensure correct results. Other methods commonly used for particle tracking are discussed in a recent practical review by Carter *et al* [68].

4.3 Results and Discussion

The apparent position of a particle stuck on the coverslip (by electrostatic forces) was measured to find an approximate value for the noise associated with the measured particle position for the two tracking methods. The high-speed video camera measured a standard deviation of 12nm and the QPD measured a standard deviation of 6nm. The difference is likely to be partly because of different susceptibility to external vibration and drift of instruments as well as electronic noise in both methods. The camera tracking would not be affected by the HeNe laser stability for example but the QPD tracking would be. It is also likely that some of the measured positional fluctuations are likely to be real Brownian movement of the particle as some residual Brownian motion can still occur when particles are bound to the coverglass.

To establish the relative performance of the two position measuring techniques, repeated measurements were carried out using $2\mu m$ diameter silica spheres suspended in water. Figure 4.2(a) shows a sample of half a second of position data obtained from the two detection methods at a weak trap power of approximately 10mW. The standard deviation of the particle position over the total sample period of 4 seconds was measured to be 52nm and 53nm by the QPD and camera respectively. Figure 4.2(b) shows the corresponding power spectrum for the total sample period of 4 seconds, again showing the close agreement of the QPD and camera data. At this power the correlation coefficient of the position data from the two techniques was approximately 0.9.

Figure 4.3 shows the correlation between the position data from the two methods at varying trap powers for 4 seconds of data taken at 2 kHz. As trap strength was increased the correlation between the two methods decreased, since the fluctuations in particle position became comparable to the noise floor of the camera.

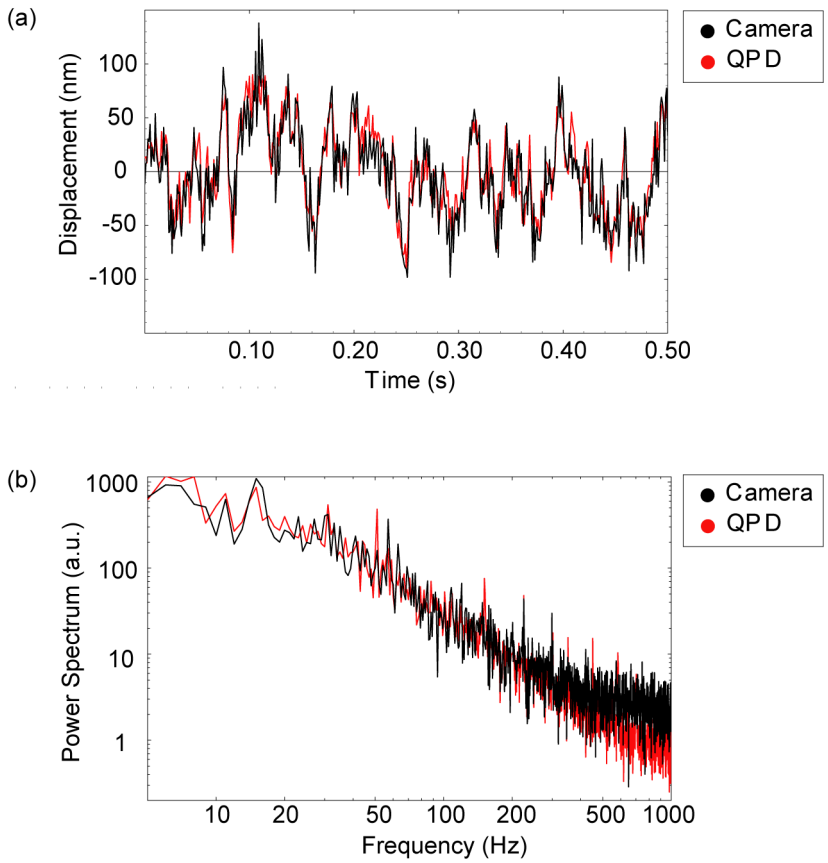

Figure 4.2: (a) A sample of position data in one axis, from an optically trapped $2\mu m$ diameter silica particle measured simultaneously with a high-speed video camera and a QPD at 2kHz. (b) Power spectrum of position data over 4 second period.

More important than the absolute correlation between the two detection techniques, is the agreement between the variance. To address this issue, the trapping power was varied and the standard deviation of the particle position plotted against the trapping power, see figure 4.4. The standard deviation is inversely proportional to the square root of the trap strength which is in itself proportional to the laser power. The experimental data from the camera and QPD show a good agreement with this prediction.

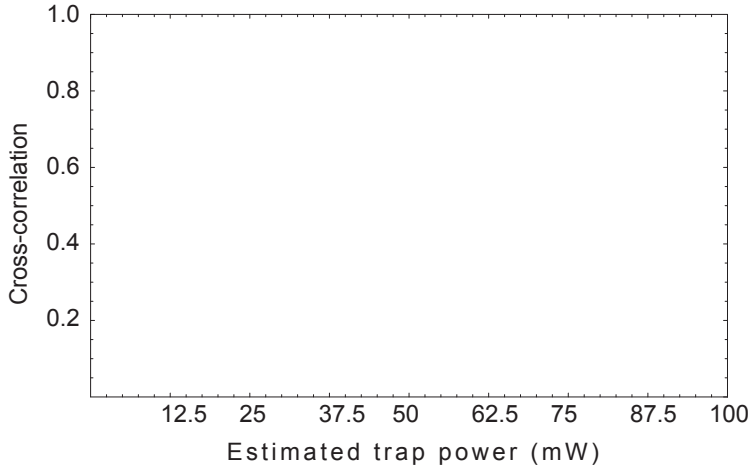

Figure 4.3: Correlation of positional data from QPD and high-speed video camera against estimated trap power.

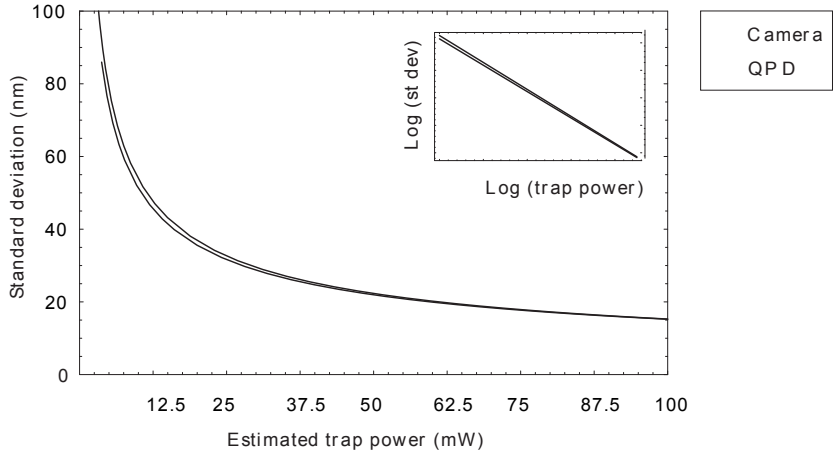

Figure 4.4: Graph showing the standard deviation in one axis recorded for a trapped particle at different trap powers. The inset shows a log-log graph of standard deviation against trapping power and corresponding fits.

4.4 Conclusions

This experiment demonstrates that a high-speed camera can be used for particle position measurement in optical tweezers with an accuracy of the order of 10nm and bandwidth of a few kHz. Although this is a lower accuracy than possible using a QPD, the high speed camera has many other

advantages. Not least of these is the ability to measure many particles simultaneously, and also the ease with which it may be calibrated. A problem that quickly became apparent with the use of such a camera, is that the size of the on-board memory buffer typically limits the duration of data capture to a few seconds. Real-time feedback of the trap strength was impossible as it took approximately 10 minutes to transfer the images from the camera buffer to the hard drive and then run the LabVIEW particle tracking software. It could be only at this point that the data may be found to look suspicious, highlighting a possible temporary problem with the setup such as an improperly sealed sample causing drift for example. This can cause inconvenience and time wasted as well as the problem of not being able to take a very long continuous run.

CHAPTER 5

Manipulation of particles with Holographic Optical Tweezers

5.1 Introduction

This chapter presents an investigation of the change in trap strength when the trap position is changed in holographic optical tweezers (HOT). The work was carried out mainly by myself and collaborator Emma Eriksson. The ability to trap and manipulate multiple colloidal particles is useful in studying the dynamics of colloidal suspensions [71] and has recently found applications in life science where parallel single cells in an array can be manipulated and studied simultaneously [72, 73]. In combination with microfluidic systems, HOT offers several new possibilities for flow measurement [74] and the ability to control the local environment of single cells in parallel [75, 76].

HOT have recently been used for optical force measurement (OFM) applications [41], using a ferroelectric SLM. HOT thus allow OFM to be applied with several trapped particles simultaneously. OFM either keeps the trap

position fixed and measures the displacement of the trapped object from the trap center, or uses the positional data to continuously adjust the trap position to bring the particle back to its initial position. The "closed loop" configuration allows a true force measurement to be performed, but requires the ability to rapidly and continuously adjust the trap position. In most closed-loop configurations the trap movement is achieved using acousto-optic deflectors (AOD).

Forces acting on the trapped particle can be measured by keeping the trap position fixed and measuring the displacement of the particle. Alternatively the trap position can be rapidly updated to attempt to maintain a stationary particle position, allowing the force to be deduced from the required displacement of the trap. Both techniques require a precise, accurate and high-bandwidth measurement of the trapped particle position.

HOT have a maximum update rate limited by combinations of technological specifications of the spatial light modulator and the computation time required to calculate the required kinoform. The diffraction efficiency of liquid crystal SLMs is high due to the many possible phase levels. However, a limitation is the slow response time of the liquid crystal. To move a trap the hologram kinoform must be updated, which takes a finite time. Depending upon the SLM specifications, the SLM display may momentarily display no hologram at all during the kinoform updating process. The minimum update of the step size possible with HOT is in the sub-nanometer range [77]. In principle it is therefore possible to move optically trapped particles with HOT in a close to continuous fashion. However, the update frequency of the SLM is, beside the technical aspects, limited by the computation time required to calculate the required kinoforms. In practice the movement of trapped objects is restricted to discrete steps.

We investigated deliberate movements of holographically trapped particles within a known fluid flow with the aim of quantifying the magnitude of the problem and establishing operating guidelines by which the performance of

a holographic optical tweezers system can be optimised. We found a highly nonlinear behaviour of the change in trap stiffness vs. changes in step size. For step sizes up to approximately 300nm the change in trap stiffness is linear. Above 300 nm the change in trap stiffness remains constant for all step sizes up to one particle radius.

5.2 Experimental Procedure

The experimental setup is illustrated in Fig. 5.1. The HOT setup is configured around an inverted Zeiss Axiovert 200 microscope with a 1.3NA,100×, Plan Neo-fluar objective. The optical traps were created using a 1.5W, 532nm C. W. laser. The laser beam was expanded to slightly overfill the SLM (Hamamatsu X8267, 768 × 768 pixels, 20 × 20mm, 256 phase levels), which was imaged onto the back aperture of the microscope objective. The kinoforms were calculated as blazed diffraction gratings to give an angular displacement of the diffracted beam and hence a lateral displacement of the trap [41].

All experiments were performed with a single 2μm diameter silica bead trapped 10μm away from the zeroth order optical trap and 5μm from the coverslip. The particle was stepped in a direction perpendicular to a fluid flow. The flow was created by translating the microscope stage with a uniform speed back and forth over a distance of 500μm, as illustrated in Fig. 5.2. The Stokes drag force of a trapped particle of radius a, generated by a fluid flow of velocity u and viscosity η is given by $F = 6\pi a u \eta$.

A halogen $100W$ light bulb and a 0.8 N.A. condenser was used to illuminate the sample, which was imaged using a CMOS camera mounted on the viewing port of the microscope. When used at its full 1280 × 1024 resolution the CMOS sensor has a standard video frame rate of 24Hz. However, by reducing the region of interest (ROI) the frame rate could be increased.

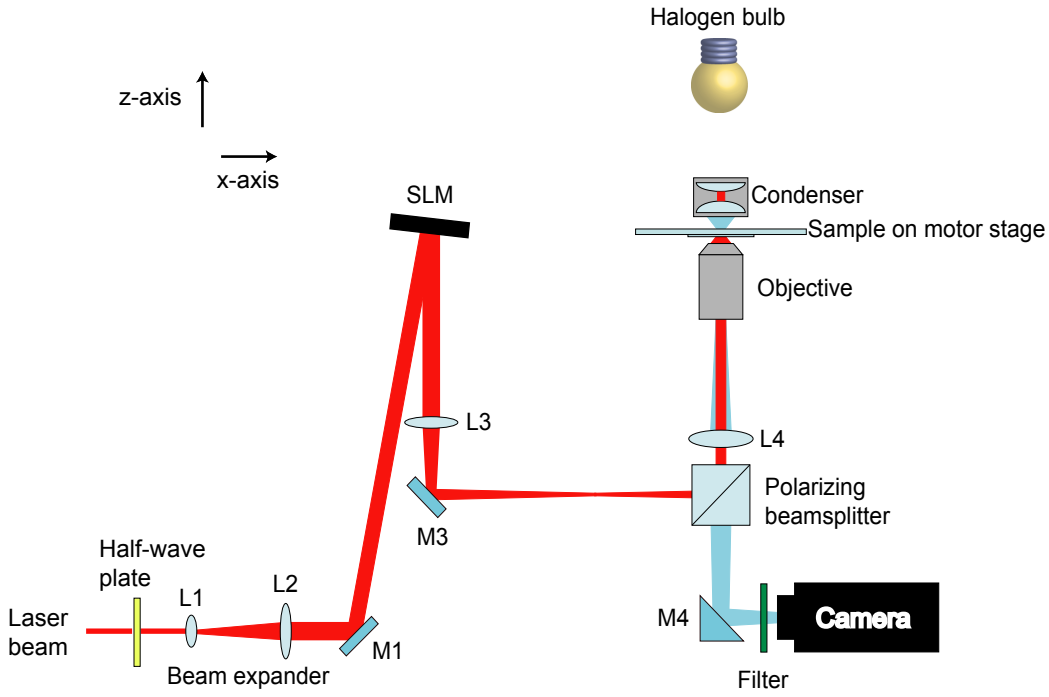

Figure 5.1: Schematic of the experimental setup used to measure the motion of a trapped particle in a fluid flow. The laser beam was expanded (lenses l1 and l2, focal lengths f1=30mm and f2=200mm to slightly overfill the SLM. A $\lambda/2$ plate was used to align the polarization of the laser to the SLM. The beam reflected off the SLM was then demagnified to fit the size of the back aperture of the microscope objective (lenses l3 and l4, focal lengths f3=600mm and f4=200mm) that focussed the light to form the optical trap. A motorized stage was used to create a flowing environment around the trapped particle. A high-speed CMOS camera was used to collect images at high frame-rate to monitor the position of the trapped particle.

For the measurements on 1.1μm and 2.0μm diameter beads the ROI was reduced to allow images to be taken at 1kHz, while the larger 5.0μm beads were imaged at 500Hz. The scale of the image was calibrated against an object micrometer. The position of the trapped bead was measured while stepping the trapped particle back and forth with a specific step size for 50s (1.1μm and 2.0μm beads) or 60s (5.0μm beads) using real-time, center-of-mass tracking with an accuracy of the order of 10nm [17]. The positional data was then analyzed to extract information about the maximum down-

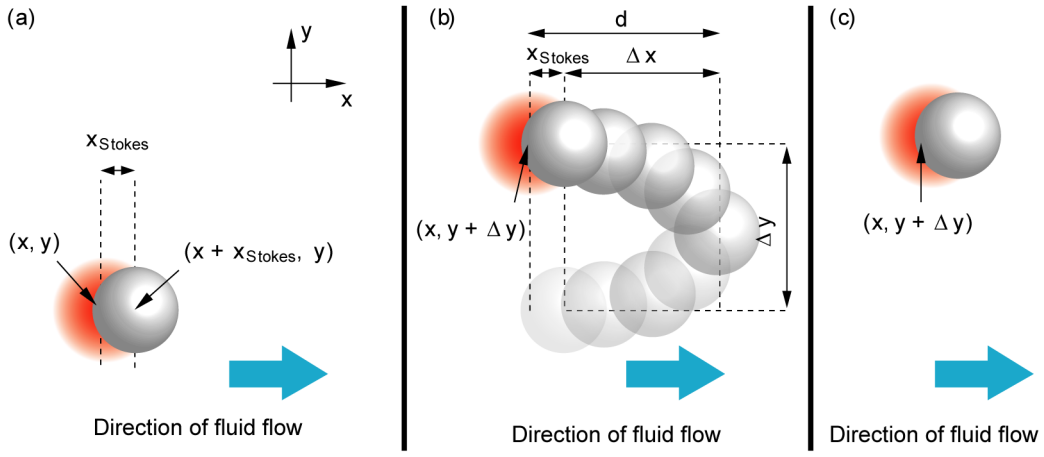

Figure 5.2: An illustration (not to scale) of using HOT to move a particle from position (x, y) to position $(x, y + \Delta y)$ in the presence of flow in the x-direction. (a) The initial position of the optical trap is at (x, y). (b) The location of the optical trap is updated to $(x, y + \Delta y)$ and the maximum downstream displacement, d, as a function of the step size, Δy, is measured. (c) The bead trapped at the new location. Courtesy of Leach [18].

stream displacement, d, during each hologram update (c.f. Fig. 5.2) and the steady state downstream displacement due to Stokes' drag. The trap position was updated at 0.5Hz, resulting in approximately 25 measurements of Δx for the smaller particles (1.1μm and 2.0μm) and 30 measurements for the larger particle (5.0μm) for each step size. The measured downstream displacements were then averaged to give one data point for each step size and particle size.

5.3 Results and Discussion

A typical example of the experimental data is shown in Fig. 5.3. For ease of illustration only 6 seconds of data are shown, 2 seconds in each of the 3 trap positions. In these plots it is possible to distinguish all the key parameters, including the steady state downstream displacement due to the Stokes' drag acting on the trapped particle (x_{Stokes}), the residual Brownian motion, the

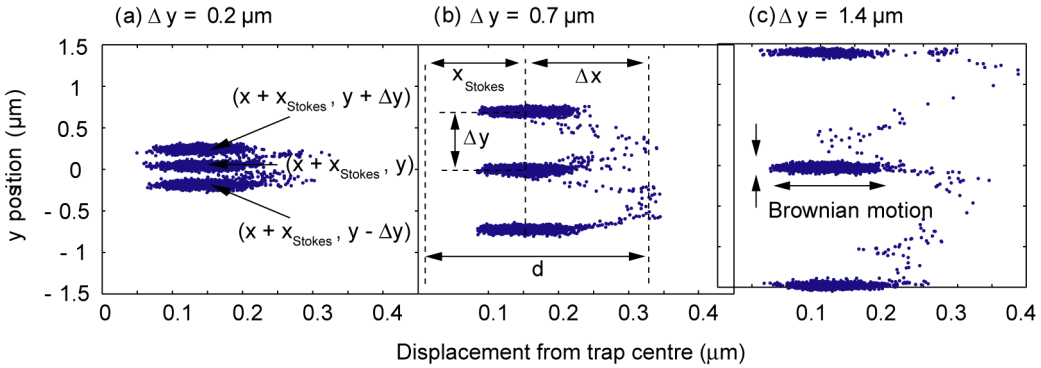

Figure 5.3: Positional data for a bead (2μm in diameter) trapped in 50μm/s flow illustrated as xy scatter plots. Data for $\Delta y = \pm 0.2, 0.7, 1.4\mu$m is shown in (a), (b) and (c) respectively. The particle is moved from top to bottom in all of the figures. Note that the displacement due to Stokes' drag, x_{Stokes}, can be seen. The aspect ratio of this diagram has been set to 7:1 in order to emphasize Δx. Courtesy of Eriksson [18].

hologram step size (Δy) and the inter-step downstream displacement (Δx) that occurs while the hologram is being updated on the SLM.

In this study we have focused on the inter-step downstream displacement relative to the center of the trap, $d = x_{stokes} + \Delta x$, as a function of particle size and step size. The experimental data of the measured displacements, d, during the SLM update are shown for three different particle sizes as a function of step size in Fig. 5.4. The behaviour is essentially the same for all three bead sizes. The downstream displacement increases with step size up to 200-300nm after which it becomes constant for step sizes up to one particle radius. For step sizes above one particle radius the downstream displacement increases again.

To explain this non-linear behaviour it is necessary to look at the intensity in the optical trap while updating the SLM with a kinoform corresponding to the new trap position. Such an intensity measurement is shown in Fig. 5.5(a), where the intensity of the laser light reflected off the coverslip was monitored with a CMOS camera in a ROI containing both trap posi-

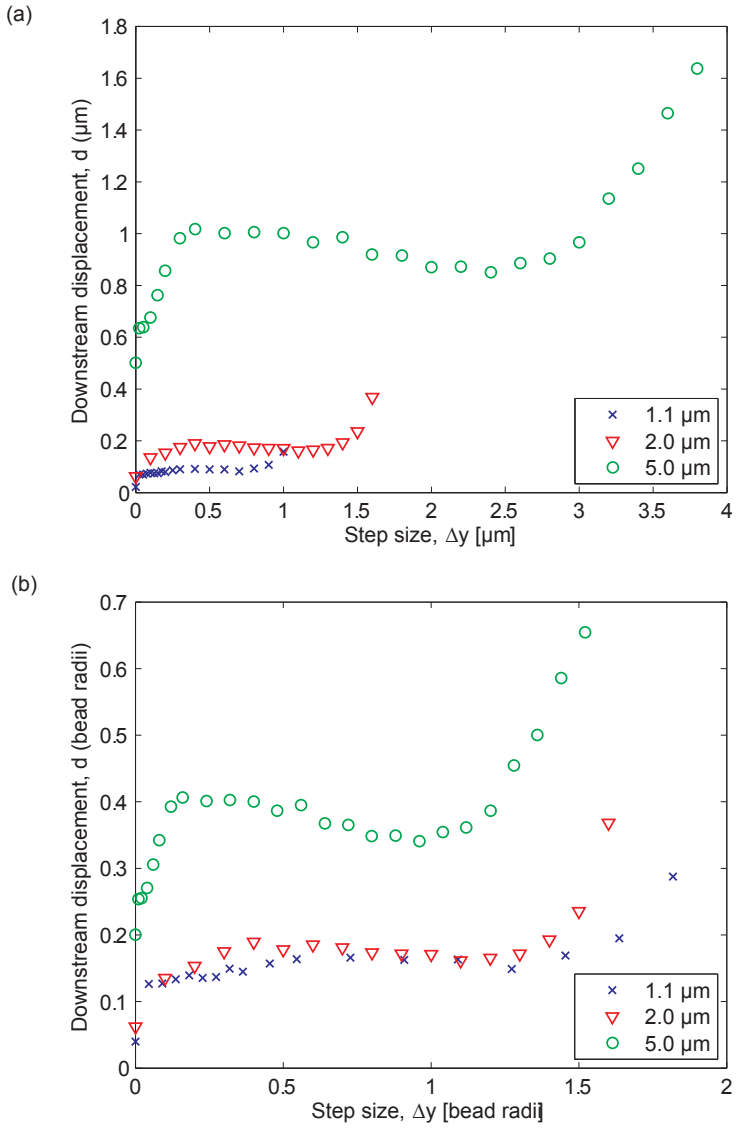

Figure 5.4: The measured downstream displacement, $d = x_{Stokes} + \Delta x$, as a function of step size for 1.1, 2.0 and 5.0μm diameter particles, subject to a perpendicular fluid flow of 50μm/s. a) Distances measured in μm and b) distances normalized to particle radii. Courtesy of Eriksson [18].

tions. The intensity measurement confirms that light is diverted away from the optical trap during the time the SLM is updating the hologram. This "dead time" was on the order of 200ms, which is also in agreement with the SLM specifications. The dead time was found to be constant regardless of

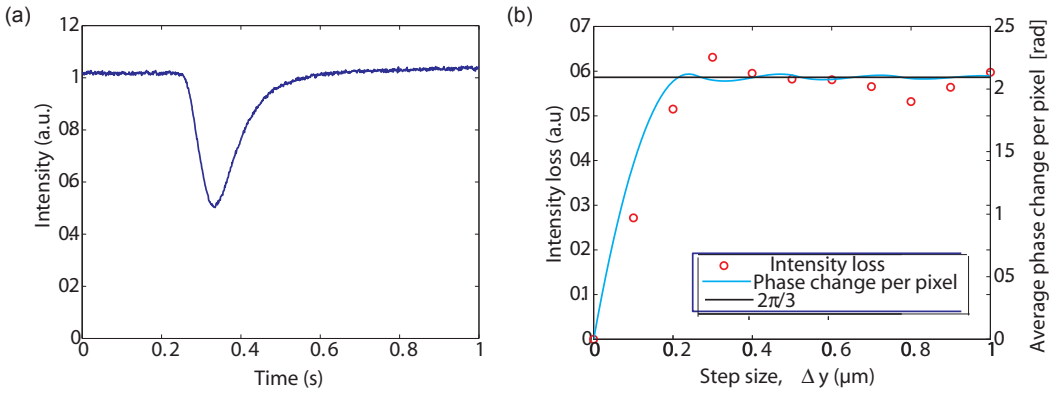

Figure 5.5: a) The measured intensity reflected off the coverslip as the SLM was updated from one hologram to another. While the SLM is updating the hologram, light is diverted away from the trapping region, thus decreasing the measured intensity. The intensity was measured in a region of interest containing both traps, when moving from $x = 10\mu$m, $y = 0\mu$m to $x = 10\mu$m, $y = 0.2\mu$m. b) Left axis (red curve): the dependence of the depth of the intensity dip on step size (steps are in the positive y direction, starting at $x = 10\mu$m, $y = 0\mu$m). Right axis (blue curve): The average phase change per pixel between two kinoforms as a function of step size (steps are in the positive y direction, starting at $x = 10\mu$m, $y = 0\mu$m), weighted with a Gaussian intensity profile. The curves saturate at a phase shift of $2\pi/3$ (black line). Courtesy of Eriksson [18].

the trap step size, whereas the intensity loss was measured to be dependent on step size (c.f. Fig. 5.5(b), left axis). The intensity loss increased up to a step size of 300nm, after which the intensity loss remained constant. This also explains why the downstream drag increases for step sizes up to 200-300nm.

Further, the behaviour of the intensity can be explained from the calculated kinoforms as the step sizes increases (the holograms are assumed to have phase values between 0 and 2π, scaling linearly with the digital signal sent to the SLM). In Fig. 5.5(b) the average phase shift per pixel when taking steps of various sizes is shown (steps are in the positive y direction, starting at $x = 10\mu$m, $y = 0\mu$m). The phase values of the different pixels have also been weighted with a Gaussian with a width matched to the size of the

SLM, in order to account for the Gaussian shape of the laser beam. The calculated average phase shift per pixel increases up to 200nm (in our setup corresponding to 1.6 grating periods across the SLM), which is in good agreement with both the intensity measurements and the measurements of the downstream displacement. It can also be noted that the average phase shift per pixel approaches $2\pi/3$ for large step sizes. This situation is equivalent to the average phase shift per pixel when changing from an arbitrary blazed grating to a hologram with a constant phase level, where the constant phase level corresponds to the *rms* value of a flat probability distribution of phase values between 0 and 2π. This explanation was further supported by measuring the downstream displacements when adding a constant phase shift per pixel to the hologram (without moving the trap position). For a range of fluid flow rates the downstream displacements for an average phase shift per pixel of $2\pi/3$ agreed well with the downstream displacements found for step sizes in the range of 300nm up to one particle radius (see fig. 5.6). As expected from the Stokes drag, there is a linear dependence of the downstream drag as a function of flow rate.

The increasing downstream drag for step sizes above one particle radius is perhaps the most intuitive part of the experimental data. The force acting on a particle is well known to fall off rapidly once the particle is more than one particle radius away from the center of the trap [78].

Finally, we also note that under the same step size and flow rate conditions the ratio of the static to inter-step downstream drag is constant for all 3 particles. This is a consequence of the drag force acting on the particles, independent of SLM performance.

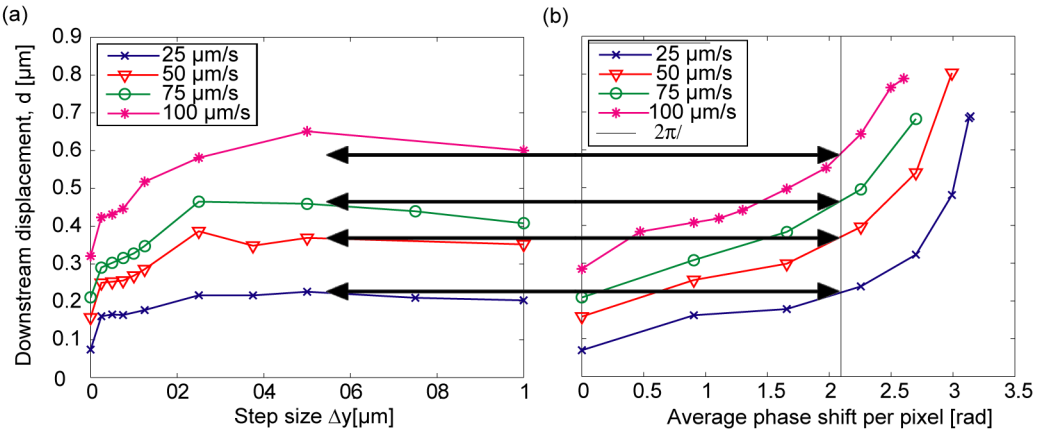

Figure 5.6: Measured total downstream displacement, $d = x_{Stokes} + \Delta x$, for four different flow rates: 25, 50, 75 and 100μm/s. The measurements were done with a 2.0μm diameter particle trapped with approximately 12mW of laser power. In figure (a) the step size was varied and in figure (b) a phase change was added to trapping hologram (without updating trap position). Note that the downstream displacements for an average phase shift per pixel of $2\pi/3$ agrees well with with the downstream displacements found for step sizes in the range 300nm up to one particle radii. Lines between points have been added to guide the eye. Courtesy of Eriksson [18].

5.4 Conclusions

When using SLMs for HOT applications one critical question is what step size should be used during particle movement. The movement of the optically trapped particle should be both rapid but not likely to result in an escaped particle. By measuring the downstream displacement in a fluid flow due to the decrease in trap stiffness during the update of the SLM we have identified some general guidelines:

1) For step sizes above the particle radius the downstream displacement during the SLM update increases dramatically, since the restoring force of the optical trap falls off quickly outside one particle radius.

2) For step sizes between 300nm and one particle radius, the inter-step

downstream displacement is approximately independent of step size. This can be explained by the decrease in trap stiffness during the SLM update, which is constant in this range. The constant intensity loss is due to a roughly constant average hologram phase shift per pixel. The data also demonstrates that the time needed for the trapped particle to travel to the new position is negligible compared to the updating time of the SLM. In addition, the downstream drag is proportional to the fluid flow rate, as expected from the Stokes drag force acting on the particle.

3) For step sizes up to 300nm (corresponding to 2.3 grating periods across the SLM), the inter-step downstream displacement increases. This is because the average phase shift per pixel in the holograms increases with the hologram step size, resulting in an increasing intensity loss during the SLM update.

CHAPTER 6

Multipoint Viscosity Measurements

6.1 Introduction

This chapter presents results of an experiment I undertook with help from Alison Yao to use a CMOS "smart camera" to track multiple particles, thus allowing viscosity measurements at multiple points within a sample. This work has recently been accepted for publication.

The emerging fields of microfluidics and lab-on-chip technology promise many advantages over conventional methods for biological and chemical measurement. The miniaturisation of micro-analytical devices results not only in a low fabrication cost and a reduction in the volume of (potentially expensive) reagents used, but also in an increased speed of analysis and the ability to run multiple analytical processes in parallel.

In recent years there have been a number of applications using optical tweezers with microfluidics, for example, to sort cells [79, 80], or to manipulate

and measure fluids within microdevices [81, 82].

In many cases the fluids being studied are complex in nature (e.g. non-Newtonian or scale dependent). Techniques used in microrheology [83] often involve introducing micron-sized particles to the fluid and tracking their thermal motion (passive microrheology) [84], providing information about rheology at the micron-scale. A variant of this method involves actively applying a force to the particles (active microrheology) to gain more information about the dynamic properties of the fluid. Active microrheology has been attempted by several means including atomic force microscopes [85], magnetic tweezers [86, 87] and optical tweezers [88, 89, 90].

Fluid viscosity has been measured successfully by various methods with optical tweezers, using a single micron sized particle as a probe [91, 92, 93, 94, 95]. Most of these approaches have inferred the surrounding viscosity by using a quadrant photodiode (QPD) to track the motion of the particle [25, 70], however, extension to many particles is cumbersome. Alternatively, it is also possible to infer the viscosity from the rotational velocity of a particle subject to a known torque [96]. This can be achieved using birefringent particles and circularly polarised light.

Recent advances in camera technology have, however, enabled a high-speed camera to be used as an alternative to a QPD to measure the positions of particles in optical tweezers [17, 34]. Cameras have the advantage of allowing the tracking of many particles simultaneously at high frame rates [20].

In this experiment we demonstrate the trapping of multiple silica beads with holographic optical tweezers to measure the viscosity at multiple points and then to probe local (effective) changes in viscosity due to the presence of walls within a microfluidic channel. We use a CMOS camera [97] to measure the x, y positions of multiple particles in two axes. Note that the integration of the center-of-mass processing means that only the particle positions are transferred to the hard drive, rather than the whole image, which allows

monitoring of up to 16 particles at several kHz without data management problems. Typically we collect positional data at a frame rate of 2kHz.

In both cases we use our results to accurately calibrate the diameter of the beads (which are known to have a standard deviation of $\sim 10\%$). Once calibrated, this offers the possibility for the precise knowledge of spatially and temporally varying viscosity distributions which allow controlling processes in colloidal systems and biological samples. In addition, the technique has the potential to create a new method for mapping microfluidic device structures /micro-landscapes.

6.2 Experimental apparatus and methods

Figure 6.1 shows the configuration of the optical tweezers, which are based upon an inverted microscope. The objective lens, 100x 1.3NA, (Zeiss, Plan-Neofluor) was mounted on a piezo-controller and used to both focus the trapping beam and to image the particles. A 50W tungsten-halogen lamp and condenser was used to illuminate the sample. Trapping was achieved using a C.W. Ti:sapphire laser system (M2, SolsTiS). The laser was expanded to slightly overfill the aperture of a spatial light modulator, SLM (Hamamatsu, LCOS X10468-02), and then coupled into the tweezers system by imaging the SLM on to the back aperture of the microscope objective lens. By appropriate hologram design, this allows multiple optical traps to be created in the sample plane. The microscope slide and cover slip, forming the sample cell, were mounted on a motorized microscope stage (ASI, MS-2000) above the objective.

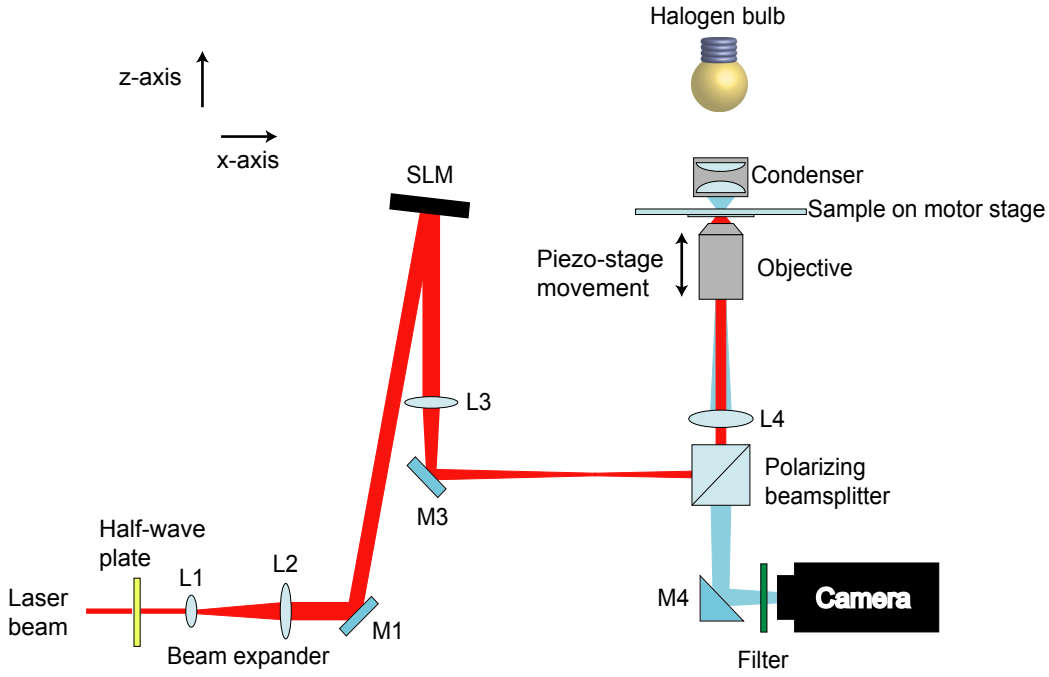

Figure 6.1: Experimental setup.

Drag coefficient modification near a surface

In the microfluidic channel used it was not possible for particles to be tens of radii away from any surfaces and changes in drag coefficient due to the presence of walls must also be taken into account. Strictly, the viscosity of the fluid is unchanged, but the modified drag coefficient does change the dynamics of the particle motion in an equivalent fashion. The change in viscosity due to walls can be precisely predicted by Faxén's correction [98, 99, 29] and a particle moving perpendicular to the wall will experience a drag coefficient, $\gamma^{\perp}$, which is related to its unbounded drag coefficient, γ_0, by:

$$\frac{\gamma^{\perp}}{\gamma} \equiv \frac{\eta^{\perp}}{\eta} = \left[1 - \frac{9}{8}\frac{a}{s} + \frac{1}{2}\left(\frac{a}{s}\right)^3\right]^{-1}, \tag{6.1}$$

where s is the distance from the wall to the mid-point of the particle and a is the particle radius. By trapping multiple particles at different distances from a microfluidic wall (see figure 6.3(b)), which can then be moved towards them, we can measure the viscosity at different positions in the channel and then use Faxén's correction to calibrate the size of the particles. Note that when trapping particles close to a microfluidic wall some disruption of the illumination occurs which may affect the particle tracking accuracy. In order that the particles could be brought to within a radius of the wall without illumination problems, larger 5μm, diameter particles were trapped (instead of 2μm). Camera field-of-view constraints then meant that only three particles could be trapped in a line so that the interparticle distance would be large enough to have little effect on the measured viscosity.

The viscosity of the fluid around each particle can be calculated by analysis of the thermal motion of the particles using either the power spectrum or autocorrelation function of the particle position as explained in Chapter 2.

The autocorrelation function of the position data allows the viscosity η to be calculated [31]:

$$\eta = \frac{\tau\, k_B T}{6\pi a \langle x^2 \rangle} \tag{6.2}$$

where $\langle x^2 \rangle$ is the mean square displacement of the particle from the trap centre and $\tau = \gamma/\kappa$ is the decay time.

Power spectrum analysis [28] can be used to calculate viscosity [91]. The power spectral density, $S_x(f)$, is a Lorentzian of the form:

$$S_x(f) = \frac{k_B T}{2\pi^2 \gamma_0 (f^2 + f_c^2)} \tag{6.3}$$

where $f_c = \kappa/2\pi\gamma_0$ is the corner frequency. By fitting a Lorentzian with the two parameters $A = k_B T/2\pi^2\gamma_0$ and f_c, η can be calculated.

In principle both approaches should give the same answer. However, in

practice, a number of parameters need to be set, ranging from the degree of thresholding of images from which the centre of mass of the trapped particle is determined, to the length of time over which data should be taken and subsequently windowed or averaged [28]. These parameters affect the viscosity calculated from the two approaches in different ways. For example, the duration of the data and how one subdivides this into shorter lengths is important due to low-frequency drift in the apparent particle position (most likely due to thermal drift in the camera mounting and laser pointing stability) [34]. We use the two approaches simultaneously in "real time" as a way of increasing our confidence in the fitting routines and the validity of our data. In both cases, the uncertainty in the radii of the trapped particles (which typically have a 10% standard deviation) limits the accuracy to which the viscosity can be calculated. By trapping multiple particles at fixed points in a bulk fluid of known viscosity we can calculate the particle sizes and hence calibrate the viscosity measurements.

6.3 Results

In the initial experiment we trapped nine 2μm silica particles in water at 27°C. The particles were arranged in a rectangular grid 10μm above the coverslip (see Figure 6.2(a)) and far from any other boundaries. Particle positions were measured for 60 seconds and the viscosity for each particle was calculated from 5 second intervals of data using Equation 6.2 and assuming that each particle had a radius, a, of 1μm. As shown in Figure 6.2 (a), the measured viscosities are distributed around the predicted viscosity of $0.85 \times 10^{-3} Pa.s$. These variations are due to the expected deviations in particle size. For a known viscosity, we can rearrange Equation (6.2) to calculate the actual radii of the particles. The percentage change from the expected value of $a = 1\mu$m for each particle is shown in Figure 6.2(b). As expected, all lie within the 10% standard deviation.

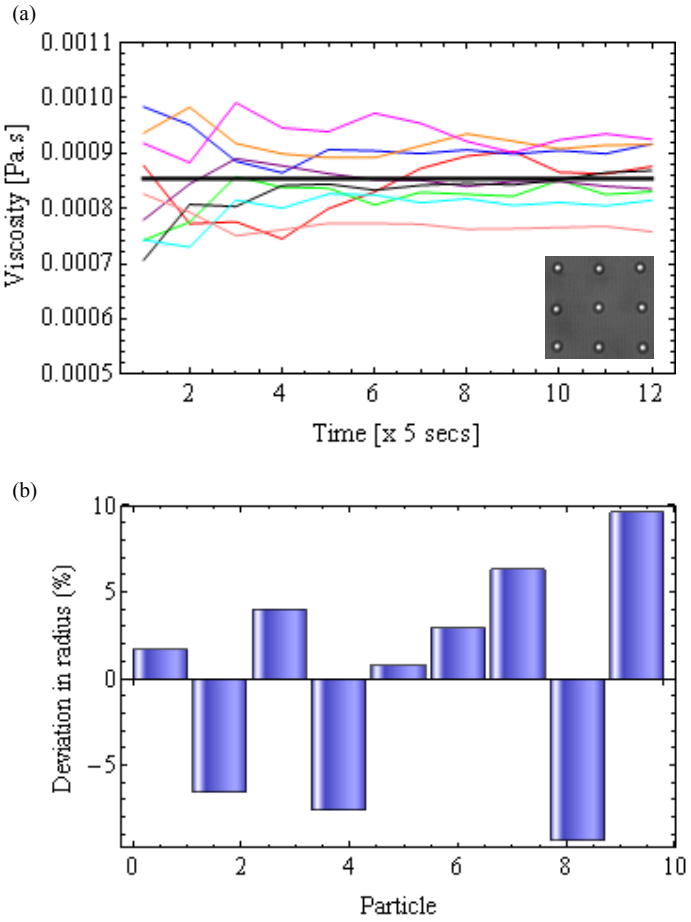

Figure 6.2: (a) Viscosity calculated from the thermal motion of nine 2μm silica particles in optical tweezers, trapped as shown in the inset. Particle positions were measured for 60 seconds and the viscosity calculated from 5 second intervals of data. The black line shows the predicted viscosity for water at 27°C. (b) Percentage deviation in particle size from $a = 1\mu m$, calculated using the predicted viscosity.

To calibrate particle size in microfluidic devices, three 5μm diameter silica particles were trapped in a sample of water within in a polydimethylsiloxane (PDMS) microfluidic channel (25μm deep) sealed with a cover slip (150μm thick). The particles were initially trapped at different distances from a microfluidic wall (see Figure 6.3(a) inset) which was then moved towards them, allowing the viscosity to be measured at different positions in the channel. Note that, as before, there may be small deviations in the size of

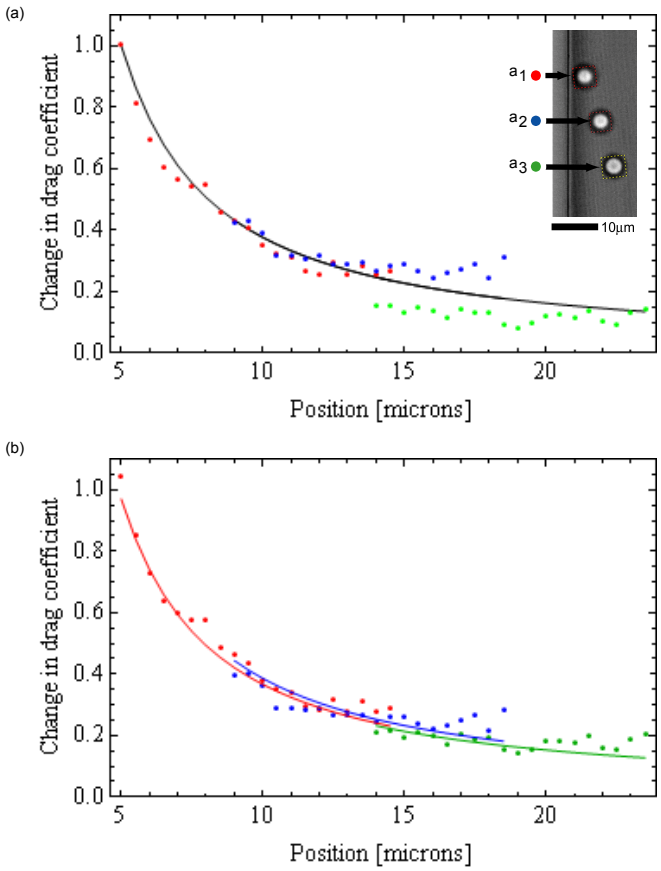

Figure 6.3: (a) Measured fractional change in viscosity for three particles at different distances from the microfluidic wall (inset) assuming $a = 5\mu m$. Solid line shows corresponding Faxén's correction. (b) Fractional change in viscosity and corresponding Faxén's correction for particles of radii $a_1 = 2.45\mu$,$a_2 = 2.55\mu m$ and $a_3 = 2.375\mu m$ against the distance of the particles from the microfluidic wall.

the particles.

Figure 6.3 (a) shows the change in effective viscosity, $\Delta\eta^{\perp}/\eta$, for each of the particles and the predicted variation (solid line), calculated using Faxén's correction in Equation (6.1), assuming the particles are all 5μm in diameter. The general agreement between measured and predicted values is good. However, the agreement is improved, as shown in Figure 6.3(c), if we take into account deviations in particle size. In this case we find the radii of the

particles to be: $a_1 = 2.45\mu$m, $a_2 = 2.55\mu$m and $a_3 = 2.375\mu$m. This method allows us to calibrate the size of particles within microfluidic devices. Once calibrated, we can then accurately measure viscosity as a function of position since we know that any further variations are due entirely to the geometry of the device.

Note that the drag force for a particle moving in the direction parallel to the wall will also increase as the particle-wall separation decreases. In this case, however, the results are significantly more affected by the hydrodynamic interactions between the particles. This was confirmed by calculating the parallel and perpendicular autocorrelation functions for an individual particle, first without any other particles nearby and then when another particle was trapped 4 radii away. For the direction perpendicular to the interparticle axis the change in the decay time due to the introduction of the second particle was less than 1%. For the direction parallel to the interparticle axis, however, the change was around 8%.

6.4 Conclusion

We have demonstrated that high-speed video imaging of the thermal motion of trapped beads allows the measurement of the viscosity of a fluid at multiple points at the micron scale. As an example of the potential of the technique to measure absolute values of viscosity, arrays of particles were trapped and tracked. The mean viscosity measured was within the expected value for the assumed temperature. Differences in viscosity/translational drag coefficient around spatially distributed particles can be measured to an error of less than 10%. We propose that such a technique could be used in colloidal systems or biological samples to allow multi-point rheology measurements. The simultaneous tracking of multiple particles also allows the small variations in particle size to be averaged out, decreasing the error from particle-size uncertainty.

CHAPTER 7

Underdamped modes in a hydrodynamically-coupled viscous system

7.1 Introduction

This chapter gives an introduction to hydrodynamic interactions between colloidal particles; followed by the details of an experiment I carried out with Dan Burnham (University of St Andrews) and David McGloin (University of Dundee). The hydrodynamic interactions between two closely trapped water droplets was investigated and the analysis was primarily carried out by Alison Yao. This chapter is based on a recently accepted paper for publication.

Although the motion of trapped, micron-sized water droplets in air are overdamped, when droplets are close enough to be hydrodynamically coupled, theory predicts that eigenmodes of the positional fluctuations can crossover into the underdamped regime. We experimentally verify the existence of

underdamped modes of two trapped water droplets in close proximity, using a CMOS "smart camera"[97].

7.2 Background

Hydrodynamic interactions have consequences on many collective phenomena such as colloidal aggregation and gel formation where attractive interactions push to modify interparticle distances [100]. Moreover particles are always subject to stochastic thermal forces whose effects may be strongly influenced by hydrodynamic interactions, as is the case with polymer dynamics [101], or for protein conformational changes [102, 103]. In three dimensional bulk fluids, the strength of hydrodynamic coupling decays with a/r where a is the particle size and r is the interparticle distance. This long range character makes hydrodynamic interactions important in determining the dynamical behaviour of colloids and poses a number of numerical and theoretical challenges to the physical modeling of such phenomena.

The dynamics of colloidal suspensions are extremely important in both industrial and biological applications [71]. Optical tweezers are becoming an increasingly useful tool in the study of colloids and hydrodynamic interactions [25, 104, 105] as they allow the positioning and tracking of individual particles, rather than the study of the bulk dynamics of a colloidal system.

One of the first applications of optical tweezers to colloidal hydrodynamics was carried out by Crocker *et al.* [67] in 1996; to measure the hydrodynamic corrections to the Brownian motion of two colloidal spheres when they are in close proximity of each other. In this case, the diffusion coefficients associated with two 0.97 micron diameter polystyrene spheres were found to change as the distance between the two particles was changed. The particles were imaged onto a standard video camera at 30Hz and subsequent particle tracking software used to track the positional fluctuations. Optical tweezers

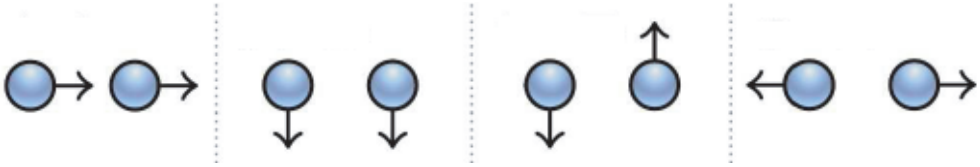

Figure 7.1: Illustration of the four eigenmodes for two particles in an overdamped system. Equal chance of fluctuations of beads being correlated or anticorrelated. However, particles relax into centre of respective traps more slowly after an anticorrelated fluctuation. Results in a time delayed anticorrelation between 2 trapped beads. Figure courtesy of Di Leonardo.

were used as a convenient tool for positioning the particles accurately.

A similar technique has also been used to show changes in diffusion coefficients of spheres when near surfaces [106, 107]. In 1999, Meiners *et al.* [25] investigated hydrodynamic interactions between two trapped particles using two quadrant photodiodes [22]. The cross-correlation function between the positions of the two particles showed a dip below zero at small timescales of a few milliseconds. Meiners shows that the result can be explained quantitatively by a model based on the Oseen superposition approximation. Physically it can be explained by asymmetry of the hydrodynamic interaction as illustrated in Figure 7.1. Each of the trapped particles exhibits residual Brownian motion so their position within their respective traps is fluctuating. After a fluctuation the particle experiences a force directed towards the center of the trap. If the fluctuations result in the two particles moving in opposite directions (anti-correlated fluctuations) then, for the particles to be pulled back into the center of their respective traps, fluid needs to be displaced between them. For a symmetric fluctuation the particles slip-stream each other back to the center of the trap which does not involve fluid displacement between the particles. Therefore, the anticorrelated eigenmodes are more highly damped than the symmetric ones and hence negative correlations persist longer, as illustrated in Figure 7.2.

To study the effects of this hydrodynamic interaction on the behaviour of more than two particles is difficult using a QPD. However, a standard frame

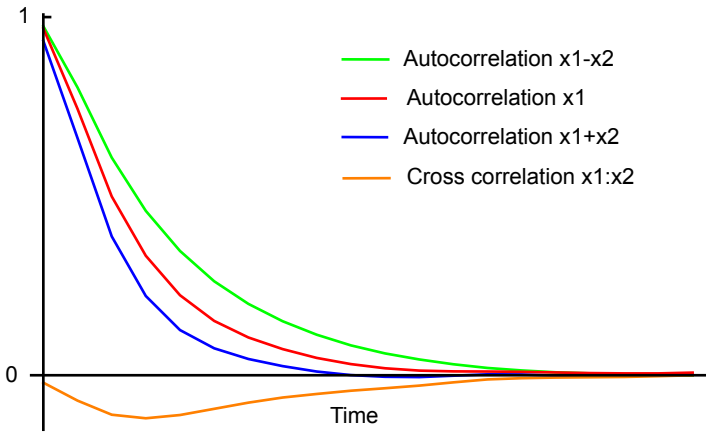

Figure 7.2: Normalised autocorrelation functions of the eigenmodes for two trapped particles, 4 radii apart. The red line is the autocorrelation function for one of the trapped particles far from other particles. The green line represents the autocorrelation function of $x1 - x2$, where $x1$ and $x2$ are the displacements of particle one and two respectively when 4 radii apart. The blue line represents $x1 + x2$ and the orange line represents the cross correlation function between $x1$ and $x2$.

rate camera is too slow to detect the effect. Polin *et al.* recently negotiated this problem by slowing down the interaction between the particles by using a medium more viscous than water (water-glycerol solution). This enabled the use of a standard camera to study how time delayed anti cross-correlations between adjacent particles affects how a 1D array of trapped particles behave and comparing to predicted results for an infinite chain [104]. Polin analyses the positions of the 1D array of particles in terms of propagating waves along the array. Polin *et al.* also predicts that more massive spheres more strongly in a lower-viscosity medium would show the crossover from overdamped dynamics to a regime of underdamped propagating elastic waves [104]). This regime was not experimentally verified due to the experimental difficulties of decreasing the viscous forces with respect to the inertial forces.

Until recently, standard methods of digital video analysis [67, 68, 108] have only allowed particles to be tracked at 10s of Hz, typically writing images to a buffer before downloading onto a computer, as mentioned in Chap-

ter 4. Recent advances in camera technology have meant that high-speed cameras can now be used to track many particles simultaneously at frame rates of several kHz for indefinite periods of time [20] thus allowing analysis of particles trapped in much less viscous media, such as air. The lower damping in air means that trapping particles is significantly more difficult than in water [109] and it is only recently that this has been extended to the holographic trapping of multiple particles [110].

7.3 Theory

The motion of a single spherical particle in a symmetric optical trap with harmonic trapping potential is described by a Langevin equation [30]:

$$m\ddot{\mathbf{r}}(t) + \gamma_0\dot{\mathbf{r}}(t) + \kappa\mathbf{r}(t) = \mathbf{F}^B(t) \tag{7.1}$$

where $\mathbf{r}(t)$ is the trajectory of a particle of mass m and radius a localized in a trap of strength κ and $\gamma_0 = 6\pi\eta a$ is its viscous drag coefficient in a fluid of viscosity η. $\mathbf{F}^B(t)$ describes the stochastic forces that arise from the thermal fluctuations in the fluid. These give rise to Brownian motion and are Gaussian random variables with mean and covariance:

$$\left\langle F^B(t)\right\rangle = 0 \quad \text{and} \quad \left\langle F^B(t)F^B(t')\right\rangle = 2k_BT\gamma_0\,\delta(t-t'). \tag{7.2}$$

The movement of one particle generates flow propagating outwards that can cause the movement of a nearby particle. At large enough distances the velocity $\boldsymbol{u}(\mathbf{r})$ of the fluid appears sufficiently uniform that a sphere i at $\mathbf{r}_i$ is simply advected according to Faxén's law [29]:

$$\dot{\mathbf{r}}(\mathbf{r}_i) = \mathbf{u}(\mathbf{r}_i), \tag{7.3}$$

where $\mathbf{u}(\mathbf{r}_i)$ is the fluid flow at i. In a many body system the velocity of the i-th particle will be the sum of two contributions: the speed that it would have in the absence of other particles $\dot{\mathbf{r}}_i$, plus an "ambient" velocity obtained as the sum of all the fluid velocities independently produced at $\mathbf{r}_i$ by other particles located at $\mathbf{r}_j$ [111, 112].

The effect of the hydrodynamic interaction is to modify the damping force acting on the particles. A system of N particles at positions, $\{\mathbf{r}_i\}$ respond to a set of forces $\{\mathbf{F}_i\}$ by moving with velocities $\{\dot{\mathbf{r}}_i(t)\}$, dictated by the N-body Oseen tensor $\mathbf{H}_{i,j}$:

$$\dot{\mathbf{r}}_i(t) = \sum_{j=1}^{N} \mathbf{H}_{i,j}\mathbf{F}_j. \tag{7.4}$$

At the limit of large interparticle separation, $\mathbf{H}_{i,j}$ can be approximated by [101]:

$$H_{ij}^{\alpha\beta} = \frac{1}{\gamma_0}\,\delta_{\alpha\beta}\delta_{ij} + \frac{3}{4\gamma_0}\frac{a}{r_{ij}}(1-\delta_{ij})\left(\delta_{\alpha\beta} + \frac{r_{ij}^{\alpha} r_{ij}^{\beta}}{r_{ij}^2}\right), \tag{7.5}$$

where the superscript α and β represent the direction of motion considered, $r_{ij}^{\alpha,\beta} = r_i^{\alpha,\beta} - r_j^{\alpha,\beta}$ is the particle separation in the α,β direction and r_{ij} is the distance between the two particles. Each component of the Oseen tensor effectively indicates the strength of the coupling between the motion of one particle in one axis, to the motion of another particle in a specific axis; as illustrated in Figure 7.3.

We introduce the equilibrium positions, or trap centres, $\mathbf{R}^0 = \{\mathbf{r}_i^0\}$, and assume that the particle fluctuations about their equilibrium positions are small with respect to interparticle distances so that $r_{ij}^{\alpha,\beta}$ is taken to be the trap separation. An array of trapped particles can be modelled as a thermally excited, damped system by combining the Langevin equation (7.1) with the Oseen superposition approximation (7.5):

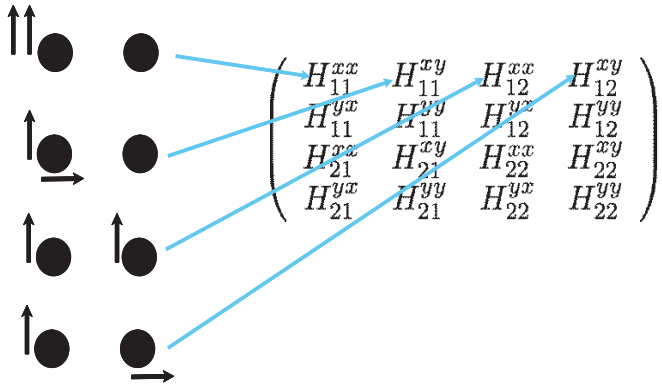

Figure 7.3: Components of the Oseen tensor for two particles.

$$m\ddot{\mathbf{r}}_i(t) + \sum_j^N \mathbf{H}_{ij}^{-1}\dot{\mathbf{r}}_i(t) + \kappa(\mathbf{r}_i(t) - \mathbf{r}_i^0) = \mathbf{F}_i^B(t), \tag{7.6}$$

where $\mathbf{F}_i^B(t)$ describes the thermal forces acting on the particle.

The motion of the particles can be analyzed in terms of the predicted eigenmodes for hydrodynamically-coupled spheres, which are eigenvectors of the Oseen tensor [29]. The time evolution of any mode can then be described by the N-body Langevin equation:

$$m\ddot{\xi}_j + \frac{\gamma_0}{\lambda_j}\dot{\xi}_j + \kappa\xi_j = f_j^B(t), \tag{7.7}$$

where λ_j is the eigenvalue associated with the mode ξ_j and the thermal fluctuations $f_j^B(t)$ are influenced by hydrodynamic interactions so that

$$\left\langle f^B(t)f^B(t')\right\rangle = \frac{2k_BT\gamma_0}{\lambda_j}\,\delta(t-t'). \tag{7.8}$$

Comparing Equation 7.7 with Equation 7.1, it is clear how the hydrodynamic interactions modify the damping force, γ_0, by an amount dependent on the eigenvalue of a particular mode of oscillation, λ_j. Correlated modes where the particles all move in the same direction have larger eigenvalues and so experience less damping force, while the opposite is true for anticorrelated modes.

Equation 7.7 has the form of a damped, driven harmonic oscillator whose general solution has a complex frequency ω_j associated with each mode given by

$$\omega_j = \frac{i\,\Gamma_j}{2} \pm \sqrt{\Omega^2 - \left(\frac{\Gamma_j}{2}\right)^2}, \tag{7.9}$$

where $\Gamma_j = \gamma_0/(m\lambda_j)$ and $\Omega^2 = \kappa/m$. There are three distinct regimes, where behaviour depends on the ratio of Ω and Γ_j:

(i) if $\Gamma_j > 2\Omega$ the system is overdamped,
(ii) if $\Gamma_j = 2\Omega$ the system is critically damped,
(iii) if $\Gamma_j < 2\Omega$ the system is underdamped.

Since Γ_j depends on the eigenvalue of a particular mode, λ_j, modes with larger eigenvalues are more likely to be underdamped. This demonstrates how the crossover from overdamping to underdamping is governed by the hydrodynamic coupling. In particular, for the system to be underdamped we require that $\Gamma_j^2/(4\Omega^2) < 1$. Rewriting this as $9(\pi\eta a)^2/(m\kappa\lambda_j^2) < 1$, we see that we can move towards under-damping by decreasing the viscosity of the fluid, increasing the mass of the particle, or increasing the trap strength.

7.4 Experimental configuration

The custom built optical tweezers is illustrated in figure 7.4. A 532nm Gaussian beam from a Laser Quantum Finesse 4W C.W. laser is expanded to fill a Holoeye LCR-2500 spatial light modulator and then demagnified via two 4f imaging systems to slightly overfill the back aperture of a Nikon Plan 100x (NA=1.25) oil immersion microscope objective lens. The wavelength of the laser beam was chosenly only for convenience and the experiment could be carried out with other wavelengths. The SLM is used to display an appropriate hologram to create two optical traps. The beam is focused through a type 1 coverslip into the sample chamber. The sample is illuminated with

a long working distance Mitutoyo 100x (NA=0.55) microscope objective lens via Köhler illumination from a halogen fibre illuminator (ThorLabs). The Nikon objective images the sample via an appropriate tube lens onto the CMOS camera. The integration of the center-of-mass processing means that it is only the particle positions that are transferred to the hard drive rather than the whole image, which allows indefinite monitoring of up to 16 particles at several kHz without data management problems. In this case we monitor at around 3.5kHz.

Droplets were produced by nebulizing a salt solution (20-80g/L) with an Omron MicroAir NE-U22 nebulizer to produce polydisperse liquid droplets with a mass median aerodynamic diameter (MMAD) of 4.9μm. Where MMAD is defined as the mass of the medium diameter of droplets when droplets are assumed to be spheres. Adding salt to the water allows the droplets to reach equilibrium with their surrounding environment at larger sizes [113], required for this experiment. There is also a positive linear dependence of captured droplet size with laser power so we use as high a laser power as possible (300-400mW)while still allowing frequent capture of droplets [110]. Note that a major hurdle in quantitative analysis is the difficulty in accurately sizing water droplets from video images alone, due not only to their dynamic nature but also to the poor definition of their edges on the video output.

The sample chamber is a plastic enclosure $\sim$ 9mm high and $\sim$ 35mm in diameter with a type zero coverslip on the top to allow illumination of the droplets from above. This chamber is placed on top of a type one coverslip and both are held down with a heavy ring of metal, preventing flex in the coverslip during stage movement. At the top of the chamber we place tissue paper saturated in distilled water to assist in creating a humid environment. The lower coverslip was treated with Decon 90 to increase hydrophilicity so any settling aerosol produces a thin uniform water layer beneath the trapping region, minimizing abberation of the trap. To control the droplet to water surface height the sample is placed on a three axis

translation stage that moves around the fixed Nikon objective. The axial translation was manually adjusted. We first focus the beam $\sim 15\mu$m above the coverslip for ease of trapping; once caught the droplet is moved away from the water surface.

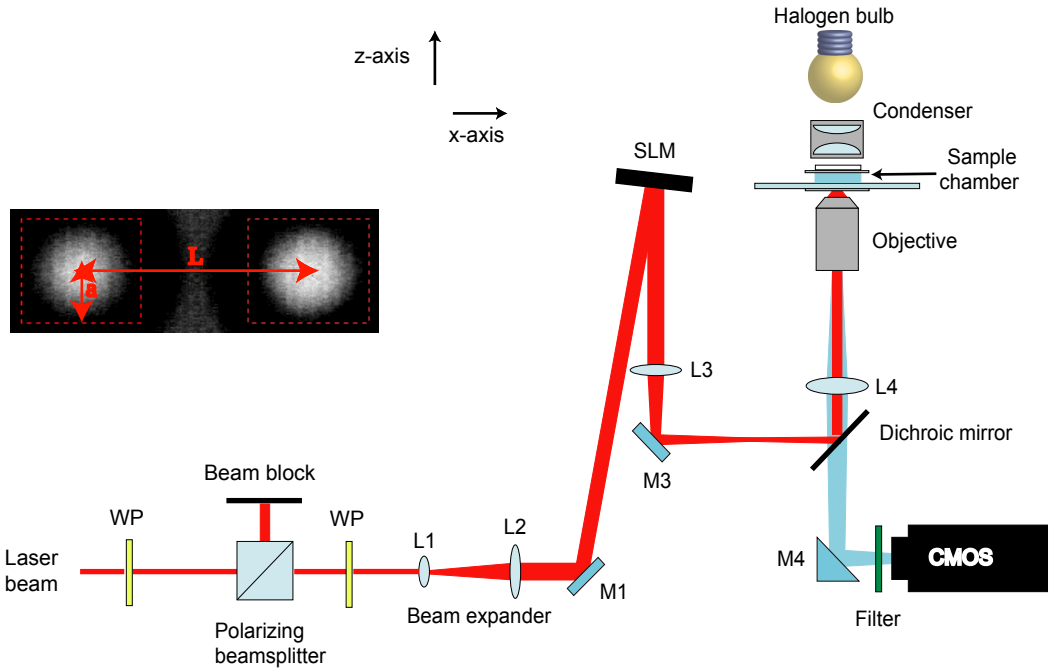

Figure 7.4: Optical tweezers setup. A Gaussian beam is expanded with lenses L1 and L2 and steered by mirrors onto an SLM and then directed by mirrors and telescope to slightly overfill the back aperture of a Nikon long-working-distance objective. Power is controlled using a polarising beam splitter and half wave plate (WP) and another WP is used to optmise the polarization of the beam for the SLM. Inset shows image of two water droplets of radius a located in optical traps separated by distance L.

7.5 Results and analysis

As explained qualitatively earlier, a two body system has 4 independent eigenmodes. If the $x-$axis is chosen along the joining line, x and y dynamics are naturally decoupled for symmetry reasons. From the measured x, y we

calculate the power spectra of the modes. The modes are eigenvectors of the matrices [104]:

$$(\gamma_0 H)^{\parallel}_{ij} = \begin{cases} 1, & i = j \\ 3a/(2r_{ij}), & i \neq j \end{cases} \quad \text{and} \quad (\gamma_0 H)^{\perp}_{ij} = \begin{cases} 1, & i = j \\ 3a/(4r_{ij}), & i \neq j \end{cases} \tag{7.10}$$

Thus, the normal modes are: $(x_1 \pm x_2)/\sqrt{2}$ and $(y_1 \pm y_2)/\sqrt{2}$ with eigenvalues:

$$\lambda^{\parallel}_{\pm} = 1 \pm 3a/(2L) \tag{7.11}$$

and

$$\lambda^{\perp}_{\pm} = 1 \pm 3a/(4L) \tag{7.12}$$

respectively. Note, x and y correspond to movement parallel and perpendicular to the line of particles, respectively, and L is the distance between them, which in this case is $\sim 15\mu m$.

We assume that the stochastic force due to thermal agitation, f^B_j, has a white noise power spectrum

$$S^B(\omega) = \frac{\Gamma_j k_B T}{\pi}. \tag{7.13}$$

Then Fourier transforming (7.7) and using (7.13) we obtain the power spectrum of mode fluctuations:

$$S^{\xi}(\omega) = \frac{k_B T}{\pi\kappa} \frac{\Omega^2 \Gamma_j}{(\Omega^2 - \omega^2)^2 + \omega^2 \Gamma_j^2}. \tag{7.14}$$

The power spectra for the modes are shown in Figure 7.5. In both cases it is clear how the particle dynamics changes from an overdamped Lorentzian spectrum for the relative mode (blue squares) to an underdamped spectrum for the collective mode (red circles) with a faster roll-off and the appearance of a resonance peak at $\omega = \sqrt{\Omega^2 - \Gamma_j^2/2}$. We note that this frequency is

lower than that for a damped but undriven oscillator; a familiar component of the theory of forced simple harmonic motion [114]. In addition, we see a bigger difference in the behaviour of the parallel modes than in the perpendicular modes, which is expected given the difference in the 'splitting' of the eigenvalues for the parallel and perpendicular motion.

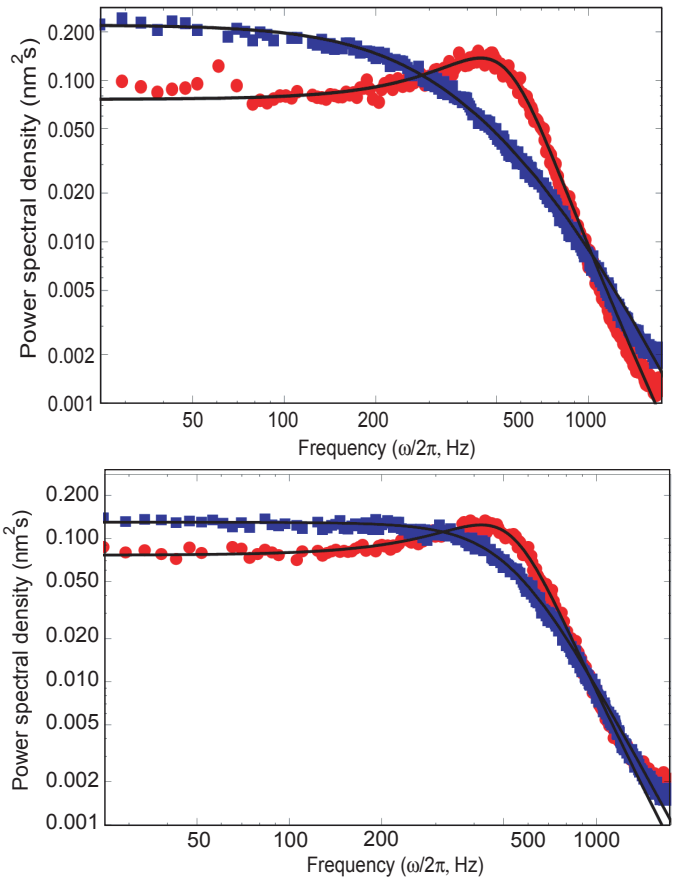

Figure 7.5: Power spectral densities for parallel (top) and perpendicular (bottom) modes of two trapped water droplets. Squares (blue) show the over-damped, collective mode. The circles (red) show the under-damped, relative mode. Solid lines show the Lorentzian fits.

By fitting these results to (7.14) we can calculate the trap frequency, Ω, and the damping coefficients Γ_j for each mode. We find an average trap frequency of $\Omega \simeq 3380$Hz, corresponding to a trap strength of $\kappa \simeq 5.98 \times 10^{-6}$pN/$\mu$m.

We can calculate the ratio of the eigenvalues from the ratio of the damping coefficients:

$$\Lambda^{\parallel} = \left(\frac{\Gamma_+}{\Gamma_-}\right)^{\parallel} = \left(\frac{\lambda_-}{\lambda_+}\right)^{\parallel} = \frac{1-\frac{3a}{2L}}{1+\frac{3a}{2L}},$$
$$\Lambda^{\perp} = \left(\frac{\Gamma_+}{\Gamma_-}\right)^{\perp} = \left(\frac{\lambda_-}{\lambda_+}\right)^{\perp} = \frac{1-\frac{3a}{4L}}{1+\frac{3a}{4L}}. \tag{7.15}$$

We find $\Lambda^{\parallel} = 0.34$ and $\Lambda^{\perp} = 0.60$ which agree very well with the predicted values of 0.33 and 0.60, respectively, calculated using the eigenvalues and an estimated particle radius, a, of $\approx 5.0\mu$m and separation, L, of 15.05μm.

As mentioned earlier, it can be difficult to accurately size water droplets from video images. Note, however, that Equation (7.15) also allows us to calculate the size of the particles from the experimental results. Rearranging, we find

$$a = \frac{2L}{3}\left(\frac{1-\Lambda^{\parallel}}{1+\Lambda^{\parallel}}\right) = \frac{4L}{3}\left(\frac{1-\Lambda^{\perp}}{1+\Lambda^{\perp}}\right). \tag{7.16}$$

Using this we calculate the radius of the particles, a, to be 4.93μm, which is very close to the estimated value of $\approx 5.0\mu$m. Using this value of a in the calculation for $\Lambda^{\parallel}$ and $\Lambda^{\perp}$ gives values of 0.365 and 0.623, respectively.

In addition to the particle size, the damping coeffcients also allow us to calculate the viscosity of the fluid, since $\Gamma_j = \gamma_0/(m\lambda_j) = 6\pi\eta a/(m\lambda_j)$. In this case we calculate the average viscosity, η, to be 2.0×10^{-5} kg/m.s which is in reasonable agreement with the expected value of 1.86×10^{-5} kg/m.s for air at room temperature (25 °C).

The effect of underdamping is to introduce a real part to the radical so that the general solution for the mode now consists of a periodic oscillation with decaying amplitude. This is clearly seen in the autocorrelation plots shown in Figure 7.6. The solid (red) lines corresponding to the collective mode in parallel and perpendicular planes are oscillatory, as would be expected for an underdamped mode. In contrast, the dashed (blue) lines, corresponding to the anti-correlated, over-damped modes show a simple exponential decay.

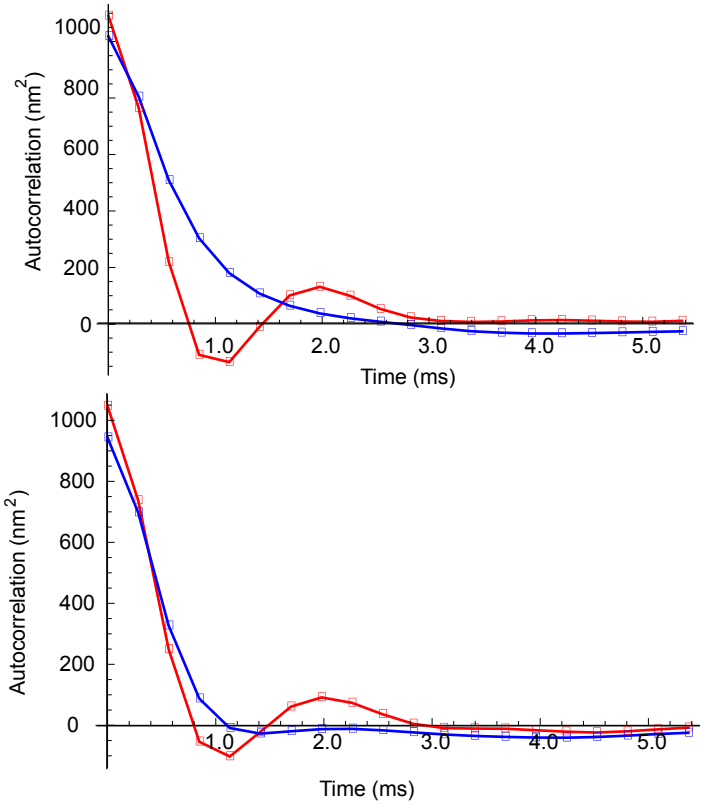

Figure 7.6: Auto-correlation curves for parallel (top) and perpendicular (bottom) modes of two trapped water droplets. Solid lines (red) correspond to the under-damped, collective mode, dashed lines (blue) are the over-damped, relative mode.

7.6 Conclusion

In conclusion, we have used holographic optical tweezers to trap two water droplets in air. By carefully tracking the positions of the trapped droplets and using the Oseen superposition approximation we were able to calculate and analyse the longitudinal and transverse modes of the system. We verified experimentally the transition from overdamped to underdamped modes and shown that this is due to hydrodynamical interaction between the particles. We expect that extension to systems with a larger number of particles would result in propagating elastic waves with anomalous dispersion and negative group velocities, as predicted by Polin et al. [104].

However, experimentally this is hampered by the difficulty both in trapping many water droplets and ensuring that they are of the same size.

CHAPTER 8

Hydrodynamic Interactions in a Two Dimensional Fluid

8.1 Introduction

This chapter presents a summary of published work [19] I carried out on a placement at Rome University "La Sapienza" with collaborators Roberto Di Leonardo and Giancarlo Ruocco. Experimental work was carried out by myself, Francesca Ianni and Roberto Di Leonardo. The hydrodynamic interactions between colloidal particles confined in a thin soap-film were studied and compared to a derivation of the two-dimensional Oseen tensor (analysis carried out by Roberto Di Leonardo). The reduced dimensions are thought to increase the range of hydrodynamic interactions compared to a bulk fluid; of relevance to diffusion and interactions of proteins in biological membranes.

It has been shown in other areas of physics that when the dimensions of a system are restricted, the result is often long range correlations arising from logarithmic decay of the field propagator with distance. One example

of this is long range Coulomb correlations and electron-lattice interactions which give rise to peculiar electronic and structural phase transitions in systems of low dimensionality [115]. In a viscous 2D fluid, the fluid flow propagator, in theory should decay logarithmically [116]. Diffusion in soap films —a quasi-2D fluid [117], are of relevance to understanding diffusion in cellular membranes [118]. There has been little experimental verification of hydrodynamic interactions in 2D fluids. Evidence for long-range dynamical correlations between an ensemble of particles in a soap-film have been reported [119]. Using video microscopy, Cheung and co-workers [119], observed long ranged spatial correlations between spheres floating in a free standing liquid film. Many-body effects were found to be significant even at very small concentrations, practically precluding the possibility of isolating hydrodynamic effects from indirect bulk measurements. Pair-wise interactions are difficult to extract from collective many-body trajectories. HOT provide a unique tool for investigation of similar systems as HOT allow the isolation of a single particle pair from other particles and boundaries. The distance between particles can be manipulated while measuring the interaction between the particles by particle tracking. Dealing with isolated pairs of particles it is possible to perform strict tests on available theories of hydrodynamic interactions. Manipulating particles with light also offers all the advantages of avoiding any physical contact with particles, which would inevitably produce a significant deformation of the liquid-air interface and dramatically affect interactions.

It is important to note that spatially confining the particles to two dimensions is not sufficient to observe these long range interactions. It is essential that the momentum flow is similarly restricted to a two dimensional plane. To this aim it is crucial that the bounding fluid has a much smaller viscosity than the film itself, a solid boundary would lead instead to hydrodynamic interactions decaying faster than in the 3D case [120].

8.2 Hydrodynamics in Flatland

As explained in Chapter 7, the motion of a particle in optical tweezers can be described by a Langevin equation [30], however, in this case the inertial term can be dropped as the viscous forces are much larger than the inertial forces:

$$\gamma_0 \dot{\mathbf{r}}(t) + \kappa \mathbf{r}(t) = \mathbf{F}^B(t) \tag{8.1}$$

If stresses produced by the fluid bounding the film (air in our case) are neglected then the variations of flow properties across the film are negligible and dynamics is governed by a two dimensional Stokes equations. This means all momentum flow is assumed to be in the plane of the film and all contributions from film surfaces are ignored. Collaborator, Di Leonardo derived a 2D form of the Oseen tensor from a 2D form of the Stokes equation to give the relation:

$$H_{ij}^{\alpha\beta} = \delta_{\alpha\beta}\delta_{ij} b + \frac{1}{4\pi\eta h}\left[\delta_{\alpha\beta}\left(\ln\frac{L}{r_{ij}} - 1\right) + \frac{r_{ij}^{\alpha} r_{ij}^{\beta}}{r_{ij}^2}\right](1 - \delta_{ij}) \tag{8.2}$$

where b is the single particle mobility, $r_{ij}^{\alpha,\beta} = r_i^{\alpha,\beta} - r_j^{\alpha,\beta}$ is the particle separation in the α, β direction and r_{ij} is the distance between the two particles. L, the film length-scale also depends on the far field boundary conditions [47].

Hydrodynamically coupled particles can then be modelled similarly to Chapter 7, by combining Equation 8.1 with Equation 8.2:

$$\sum_{j}^{N} \mathbf{H}_{ij}^{-1} \dot{\mathbf{r}}_i(t) + \kappa(\mathbf{r}_i(t) - \mathbf{r}_i^0) = \mathbf{F}_i^B(t), \tag{8.3}$$

where $\mathbf{F}_i^B(t)$ describes the thermal forces acting on the particle.

In contrast to previous derivations of Equation 8.2, Di Leonardo has included the length-scale L of the film, which is affected by the boundary

conditions assumed. As explained in Chapter 7, a two body system can be fully characterized by 4 eigenmodes as illustrated in Figure 7.1. The mobilities, λ, of the four eigenmodes as a function of interparticle distance r are:

$$\lambda_{\pm}^{\parallel} = b\left[1 \pm \frac{1}{4\pi\eta h b}\ln\frac{L}{r}\right] \tag{8.4}$$

$$\lambda_{\pm}^{\perp} = b\left[1 \pm \frac{1}{4\pi\eta h b}\left(\ln\frac{L}{r} - 1\right)\right] \tag{8.5}$$

The two parameters b and L are the single particle mobility(inverse of drag coefficient) and film length-scale, respectively.

8.3 Experimental method

The validity of the form of the 2D Oseen tensor derived can be checked by observing the dynamical behaviour of two colloidal particles confined in a free standing liquid film.

In order to directly observe 2D hydrodynamic interactions, latex beads (2 μm diameter) were dispersed in a water-glycerol mixture with 0.2% wt SDS surfactant added. A thin film was obtained by sweeping the solution on a square frame (6 mm side) of nylon wires (60 μm thickness) [121], as shown in Figure 8.1(a) with a close up of the film cross-section in 8.1(b). Glycerol increases viscosity and slows down both drainage and evaporation, resulting in longer lived films. Starting with a 50% wt water/glycerol film and then heating to evaporate most of the water, we obtained a very viscous film with a few micron thickness. We measured the film thickness at the beginning and at the end of the reported experiment to be 3.9 μm. Special care was taken with preparation and handling to avoid dust and other particles which may distort the film interfaces. Flow currents after drawing the film tend to move free floating particles towards the borders leaving the central part of the film clear of particles. The free standing liquid film was enclosed in a humidity chamber and placed over a 40x NA 0.75 objective of an inverted

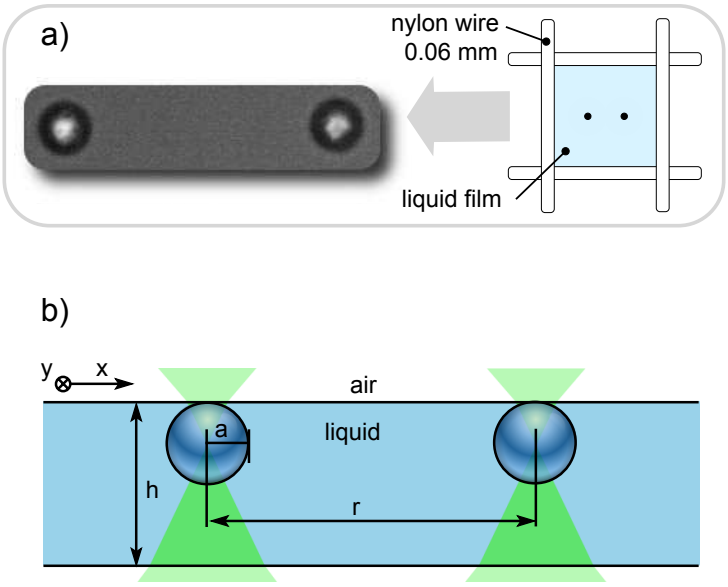

Figure 8.1: a) Shows an optical image of the trapped particles and an illustration of their orientation within a soap film drawn across a wire frame. b) Shows two trapped particles separated by r in a film of thickness h. Figure courtesy of Di Leonardo [19].

optical microscope (Nikon TE2000-U). The same objective is used to focus the laser beam (λ=532 nm) diffracted off a spatial light modulator (Holoeye LCR-2500) into two, dynamically reconfigurable, optical traps [48, 47]. Two particles were trapped and dragged to the central region to carry-out the measurements far away from menisci. Axial confinement is by capillary force on the top surface of the liquid film.

In contrast to previous studies of hydrodynamic interactions in 3D [25, 104, 20], where mobilities of eigenmodes were extracted from the correlated fluctuations of optically trapped particles, we chose to measure the eigenmode mobilities by directly exciting the four eigenmodes by moving the traps. For each of the four eigenmodes, we calculated the two holograms producing two sets of traps slightly displaced along the selected eigenmode. The two holograms are alternately displayed onto the SLM. If the SLM is fully refreshed with the new hologram in a time interval faster than the time scale of the particle dynamics, the two particles will be displaced from the

new equilibrium positions along the selected eigenmode. In this case the refresh time of the SLM is 50 ms, which is much faster than the particle dynamics.

8.4 Results and Discussion

We chose ten logarithmically spaced interparticle separations between 5 μm and 100 μm and drove the two particles back and forth (eight times) along each of the four eigenmodes. At the moment the trap positions are stepped a set distance (amplitude, ϵ) along the eigencoordinate, $\mathbf{e}_n$, the displacement, $\delta\mathbf{R}$, of the eigenmode, $\mathbf{e}_n$, from equilibrium, changes with time according to:

$$\delta\mathbf{R} = \epsilon \exp[-\kappa\lambda_n t]\mathbf{e}_n. \tag{8.6}$$

We can directly obtain the corresponding mobility λ_n by monitoring the amplitude ϵ of the $\mathbf{e}_n$ mode relaxing to equilibrium.

Particle coordinates were digitally extracted from video frames at 144 Hz. Eigencoordinates where then calculated and averaged over the eight iterations. Figure 8.2 shows the time evolution of the four eigen-coordinates at four selected interparticle distances. The two x and y correlated motions are much more mobile than the corresponding anticorrelated motions. This behaviour remains clearly visible up to the highest investigated distance (100 particle radii). The four eigen-mobilities corresponding to the four probed modes can be extracted by fitting the eigenmode dynamics to Equation 8.6. To correct for trap strength κ variations, for each distance, we normalize the four obtained decay rates to their average value. The relative eigen mobilities are shown in Figure 8.3 as a function of the particle separation. The strength of hydrodynamic coupling, reflected in the splitting of mobilities, decays logarithmically slowly with distance. Still at

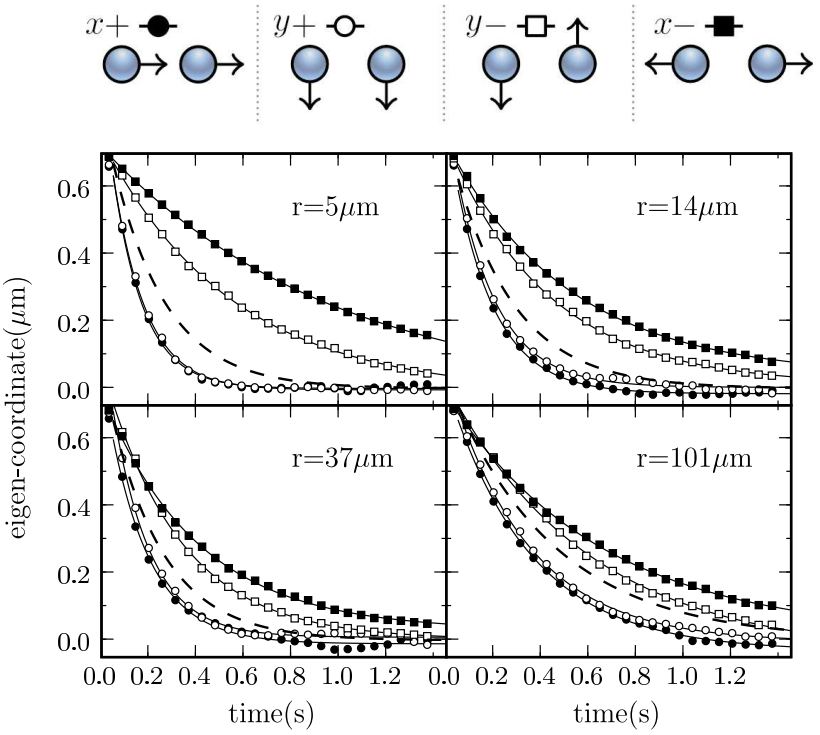

Figure 8.2: Positional plots showing the relaxation of the 4 eigenmodes for 2 particles in a soap-film, after an applied pertubation. Solid lines are exponential fits. Dashed lines represent the average single particle dynamics. Courtesy of Di Leonardo [19].

a separation of 100 radii, particles move twice as fast when forced along the same direction rather than in the opposite. At the same large separation, three dimensional mobilities would only differ by 1%.

The four data sets in Figure 8.3 can be very well fitted by Equation 8.4 leaving L and the adimensional mobility $b* = 4\pi\eta hb$ as the only free parameters. We obtain as best fit parameters $b* = 8.7$ and $L = 2.1$ mm, the corresponding fitting curves are shown as straight lines. As expected, the relevant length scale L is determined by the finite film size. In particular a sticky boundary condition on a ring inscribed in the film frame ($L_1 = 3$ mm) would give an $L = 1.8$ mm. For the same boundary condition, the single particle mobility b can be calculated for a cylinder of height h, the

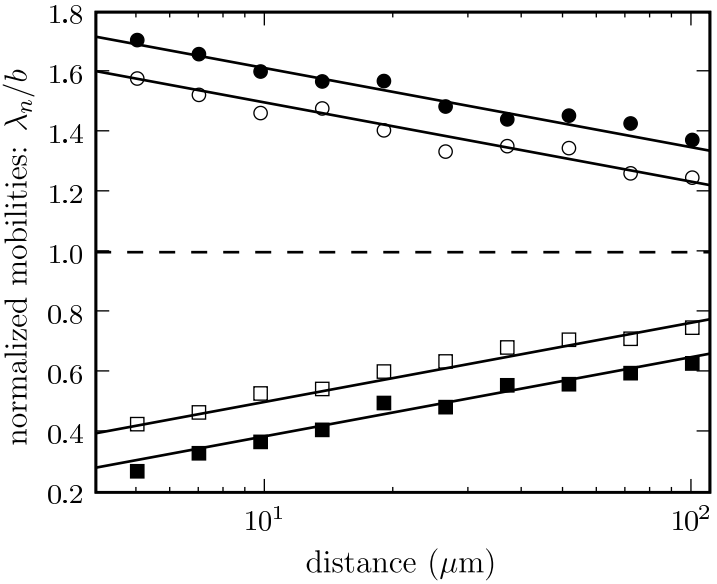

Figure 8.3: The four eigen-mobilities of a two particle system arranged at different particles separations. To correct for variations in trapping power for each distance, mobilities have been normalized to their average. Courtesy of Di Leonardo [19].

film thickness [29]. Using our particle radius a as the cylinder radius we obtain $b* = \ln(L_1/a)) - 1 = 7$ which compares reasonably well with the corresponding fitted value. We do not expect the two values to be in better agreement since the mobility b depends on the details of the boundary conditions on the particle surface.

8.5 Conclusion

As in the three dimensional case, hydrodynamic interactions produce a splitting in the spectrum of mobilities. The splitting is symmetric about the average single particle mobility and is larger for parallel than for perpendicular modes. In three dimensions, the splitting decays as a/r, falling below 10% when particle distance grows beyond 10 times the particle size a. The dependence on distance, in the two dimensional case, occurs only through

a logarithmic term, which makes hydrodynamic interactions practically unavoidable. We have shown that the hydrodynamic interactions between colloidal particles in 2D systems vary dramatically from those observed in bulk fluids. The reduced dimensionality compared to the bulk situation results in flow fields decaying logarithmically so that significant interactions between particles occur at much longer lengths. These results have particular relevance when considering diffusion and interactions of proteins in biological membranes.

CHAPTER 9

Eigenmodes of hydrodynamically-coupled multi-particle ring

9.1 Introduction

In this Chapter we demostrate the use of the "smart camera" to detect the hydrodynamic coupling between a ring of trapped particles at 500Hz. The ring can be analysed in terms of the predicted eigenmodes by using the Oseen superposition approximation [29] as in Chapters 7 and 8. Experimental work was carried out by myself, Chris Saunter (Durham University) and Jonathan Leach. Results were primarily analysed by Roberto Di Leonardo (Rome University), who compared the experimental results to the predictions of an approximation using the Oseen tensor. This work was published [20].

For systems with multiple particles, hydrodynamic effects become very important to the overall behaviour of the system. Though the two body prob-

lem can be solved theoretically, many-body effects are still at the center of active debate [122]. Optical tweezers in conjunction with high-speed video microscopy are a useful tool for gaining better understanding of multiparticle colloidal hydrodynamics.

The ring forms an array of hydrodynamically-coupled particles that can be modelled similarly to Chapter 7, although the inertial term can be dropped in this case as none of the eigenmodes would be expected to be underdamped. Equation 9.1 can be solved in the same way as in Chapter 2 Equation 2.9, to find the autocorrelation function $\langle \xi_j(t)\xi_j(0)\rangle$ of the mode:

$$\langle \xi_j(t)\xi_j(0)\rangle = C_j(0)e^{-t/\tau_j'} \tag{9.1}$$

where the variance $C_j(0) = k_BT/\kappa$ and the decay rate $1/\tau_j' = \kappa\lambda_i/\gamma_0$.

For identical traps and vanishing hydrodynamic interactions ($a/r \to 0$), the diagonal elements of $\mathbf{H}$ would be $1/\gamma_0$ and all of the off-diagonal elements would be zero. The decay rate of the autocorrelation function for each of the predicted modes was calculated. The independence of the eigenmodes were checked by calculating the cross correlation between eigenmodes.

Figures 9.1 and 9.2 show the 16 predicted eigenmodes for an eight particle ring, the known eigenmodes for a periodic chain, and how these modes map onto a ring. Alternatively, the ring can be modelled as a periodic one-dimensional chain, which has eigenmodes that are sine and cosine functions for both lateral and axial modes. The mode periods are rational fractions of the chain period and have a short wavelength cutoff determined by the particle spacing.

9.2 Experimental Method

When recording video at high-speed, brighter illumination is needed to acquire images. To improve illumination a higher NA (0.8) condenser was

used. A holographic filter was used to prevent the scattered 532nm laser light from reaching the camera, allowing nearly all the transmitted illumination light to the camera. These improvements were enough to allow recording at 500Hz with adequate image quality.

We trapped eight $2\mu m$ particles in a ring of traps using a basic holographic optical tweezers setup. A recent paper by Bechinger et al showed distortion of the location of the intensity peak of trapped particles when their surfaces are closer than one particle diameter [123]. For this reason particles were held far enough apart to avoid this effect. The positions of the particles were collected over tens of minutes and analysed off-line in terms of the predicted eigenmodes. Using the Oseen approximation we numerically calculate the eigenvalue (i.e. damping) spectrum of the eigenmodes predicted for a ring, and compare this to that analytically calculated for a periodic 1D linear chain. We used an SLM (HoloEye LCR 2500), placed in the Fourier-plane of the sample. The trapping laser (Opus, LaserQuantum) emits up to 2.0W at 532nm, which after diffraction from the SLM and transmission through the 1.3NA x100, Plan Neofluar objective lens resulted in 500mW distributed between the optical traps.

An issue associated with using SLMs is that the trap intensity can vary depending on the number of traps and their positions. The hologram kinoform was calculated using a modified [47] Gerchberg-Saxton algorithm [112] that results in trap strength standard deviation of less than 10%. Each of the traps' strength were also checked by analysis of the thermal motion of the trapped particle. Eight $2\mu m$ diameter silica beads were suspended in water and trapped to form a ring, approximately $25\mu m$ above the cover slip. The particle positions were continuously measured using a center of mass algorithm on background subtracted images, Figure 9.3, with an accuracy of order 10nm [67, 68, 17]. The x-y positions for the trapped particles were continuously logged over several minutes.

9.3 Results and Discussion

Figure 9.4 shows the measured autocorrelation functions of the eigenmodes of the eight particle system numerically analyzed as a ring and analytically analyzed as a 1D periodic chain. The straight line nature of the log-plot, together with the absence of significant cross correlations, confirms both the ring and periodic chain analyses give reasonable approximations to the real system and neither the finite particle size nor the geometric mapping of the ring onto the periodic chain lead to major deviations in the eigenmodes.

However, a more detailed examination of the eigenvalue spectrum, i.e. the damping rates of the eigenmodes, reveals some significant differences. Figure 9.5 shows the measured eigenvalues of the eigenmodes for the ring and a 1D periodic chain, of eight particles. In both cases, to allow for slight measurement uncertainty in the magnification of the image, the precise geometry of the particles is scaled by a few percent to given best agreement between the predicted and observed highly damped modes. Since, many of these highly damped eigenmodes of the ring and periodic chain are similar or identical in form, not surprisingly, both analyses yield similar eigenvalues.

The largest discrepancies between the treatments occurs for eigenmodes 15 and 16 of the periodic chain whose corresponding eigenvalues, in the Oseen approximation, diverge as the logarithm of the chain length (strictly, for an infinite chain length these modes are undamped). Eigenmode 16, the common axial motion of the chain, maps onto azimuthal rotation, which is eigenmode 14 of the ring. Eigenmode 15, the common lateral motion of the chain, maps onto a radial stretch, which is eigenmode 6 of the ring. More generally we see that for the highly damped modes where hydrodynamic forces are dominated by nearest neighbour interactions, the agreement between analyses for the ring and the periodic chain is high. For the low damped modes in which neighbouring particles move in similar directions, the forces between distance particles are more significant. In these cases coupling across the diameter of the ring perturbs the dynamics. The biggest

discrepancy in the observations for the ring occurs for the common motion eigenmodes, which we suspect are perturbed by mechanical noise within the laboratory.

9.4 Conclusion

This experiment demonstrates that the "smart camera" used has enough precision to accurately resolve the weak hydrodynamic coupling between an array of trapped particles. We have demonstrated the sensitivity of the technique by using it to analyze the eigenmodes of a trapped ring and consider how close an approximation these are to those of a periodic 1D chain. Though interparticle distances are only about three diameters, Oseen theory, applied to the ring, succesfully predicts the experimental eigenvalues to better than 2%. We find that the equivalence of ring and chain is superficially close but there are also differences. The most obvious difference arises for the modes with lowest damping, for which coupling between particles across the diameter of the ring becomes significant, increasing significantly the damping of these modes. Beyond applications in the study of hydrodynamic coupling, the high-precision, high-bandwidth multiparticle measurements made possible using these "smart cameras" opens the opportunity for multipoint photonic force microscopy [24].

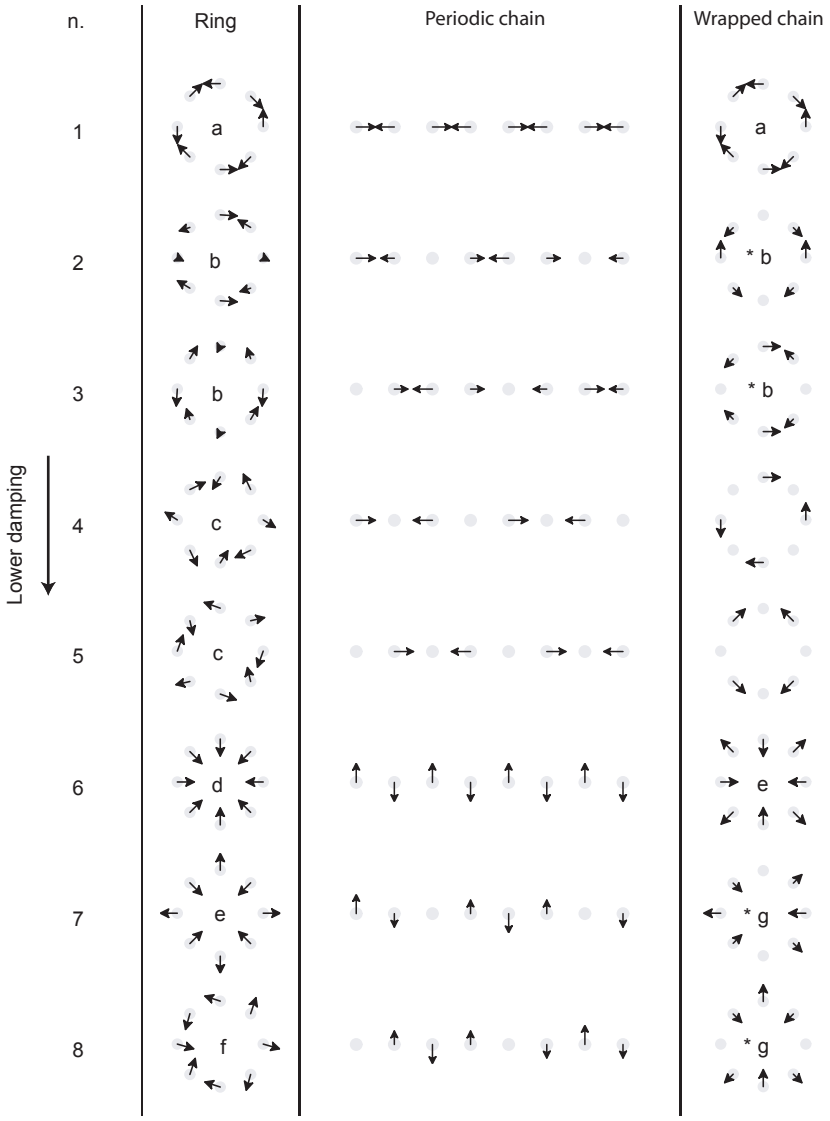

Figure 9.1: The first 8 eigenmodes predicted using the Oseen approximation for the ring, a periodic 1D chain, and the chain coordinate mapped onto a ring. The column n is the eigenmode index and they are arranged in order of damping. The ring eigenmodes are labelled with letters and $'*'$ denotes degnerate modes. These modes are cross referenced to those of the periodic chain, many of which occur in a different position with the eigenmode spectrum.

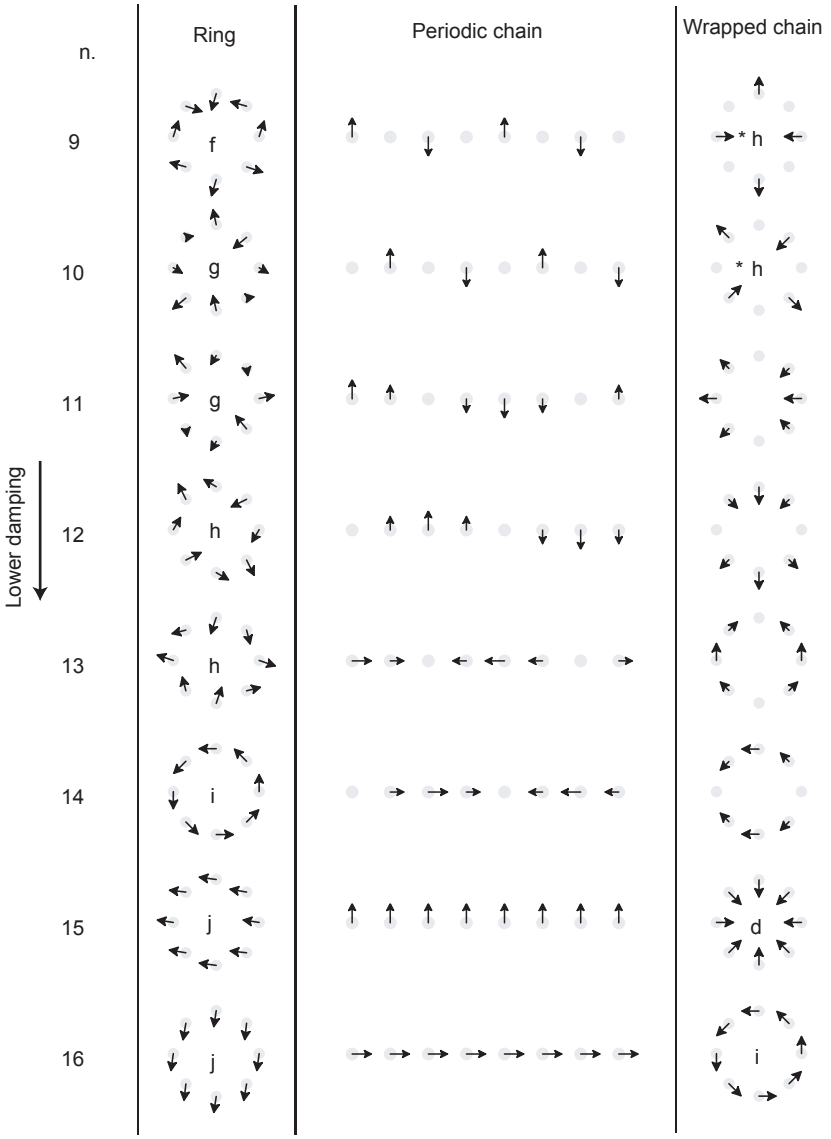

Figure 9.2: The second 8 eigenmodes predicted using the Oseen approximation for the ring, a periodic 1D chain, and the chain coordinate mapped onto a ring. The column n is the eigenmode index and they are arranged in order of damping. The ring eigenmodes are labelled with letters and $'*'$ denotes degnerate modes. These modes are cross referenced to those of the periodic chain, many of which occur in a different position within the eigenmode spectrum.

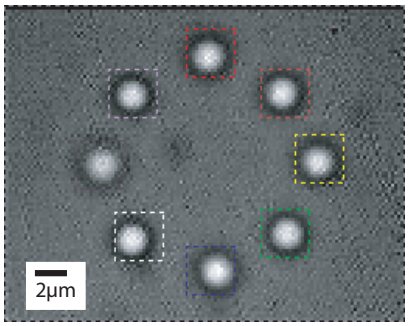

Figure 9.3: A ring of eight particles held by optical tweezers. The squares show regions of interest within which the particles' positions were monitored using a high speed camera.

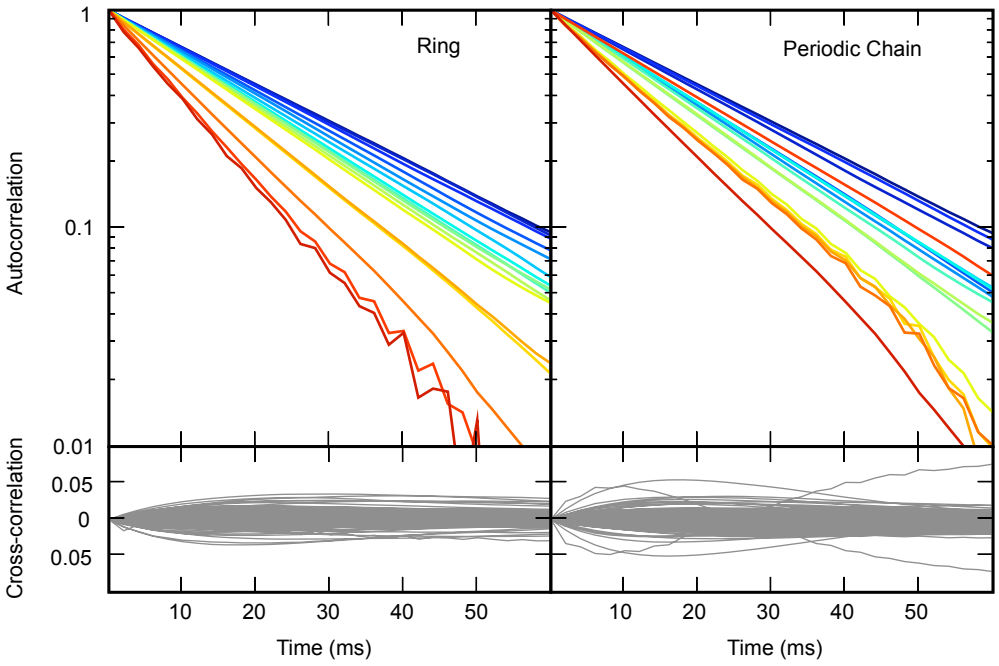

Figure 9.4: The 16 measured autocorrelation functions for the predicted eigenmodes for the eight particle ring and the eight particle periodic chain. The slowest decaying eigenmodes correspond to common motion of the particles, and hence are strongly perturbed by the mechanical noise in the laboratory. The lower panels show the, near -zero, cross correlation functions between the eigenmodes. Courtesy of Di Leonardo.

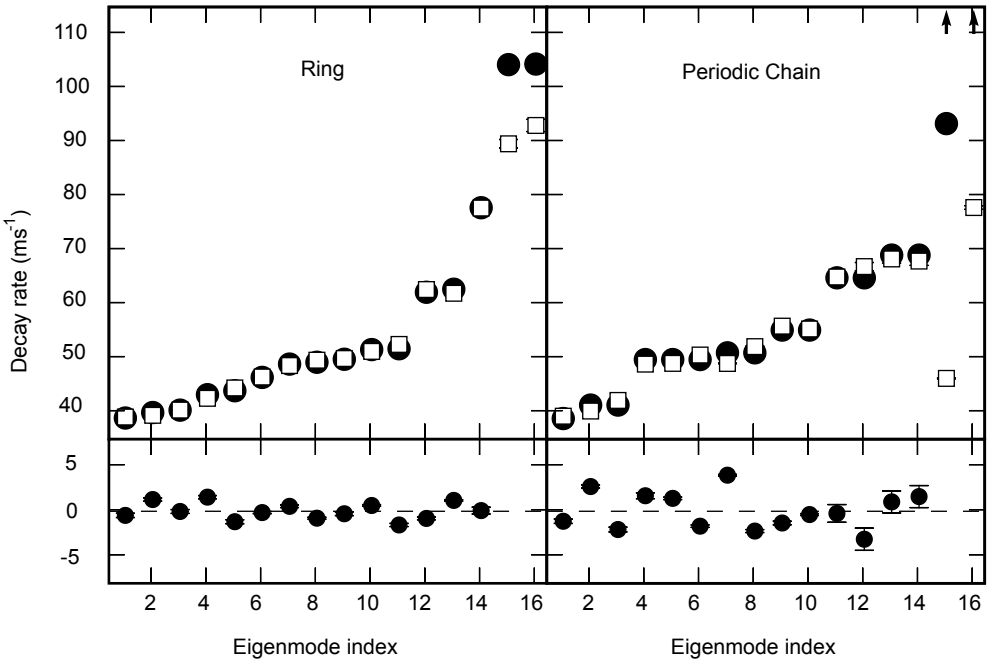

Figure 9.5: Experimental (white squares) and predicted (black circles) decay rates for the eigenmodes of a ring and a 1D periodic chain of eight trapped particles subject to hydrodynamic coupling. Courtesy of Di Leonardo.

CHAPTER 10

Conclusion

This thesis demonstrates the successful use of high-speed video cameras in optical tweezers to measure particle position at comparable accuracy and bandwidth to QPDs. This enables the convenient calibration of the QPD system against the camera, as well as allowing a simple method of tracking multiple particles at high-speed.

We have demonstrated the potential for high-speed tracking of multiple particles to probe the local environment at multiple points to detect spatial, as well as temporal changes in the fluid rheology. This opens the potential for monitoring rheological changes at multiple points within a biological sample for example.

The Durham Smart Imaging 'smart camera' has shown enough precision to accurately resolve the weak hydrodynamic coupling between an array of trapped particles, at high-enough bandwidth to track colloidal particles in water and air. This provides a useful tool for experimentally testing theories about colloidal interactions.

Currently, in the Optics Group at the University of Glasgow, progress is being made tracking the position of multiple cells with high-speed CMOS

cameras to measure the force (biological in origin) between the cells. Much progress has also been made improving the user-interface. Experiments have been carried out using a touch-screen interface in collaboration with Bristol University to control the location of multiple traps in 'real-time'. The kinoform calculation speed has recently been upgraded by using a PC graphics card instead of the central processor unit, which has allowed trap positions to be updated at (up to) 60 Hz.

It seems likely that continued improvements in HOT manipulation and 'smart camera' technology will allow more sophisticated particle tracking. The tracking of multiple non-spherical particles and inhomogenous refractive index particles in different axial planes remains a challenge which could have many uses in biological systems.

References

[1] K O'Holleran. *Fractality and topology of optical singularities.* PhD thesis, University of Glasgow, 2008.

[2] Infoplease. Comets. *Pearson Education*, 2007.

[3] A. Ashkin. Acceleration and trapping of particles by radiation pressure. *Phys. Rev. Lett.*, 24:156–159, 1970.

[4] S. Chu, J. E. Bjorkholm, A. Ashkin, and A. Cable. Experimental-observation of optically trapped atoms. *Phys. Rev. Lett.*, 57:314–317, 1986.

[5] A. Ashkin, J. M. Dziedzic, and T. Yamane. Optical trapping and manipulation of single cells using infrared-laser beams. *Nature*, 330:769–771, 1987.

[6] K. Svoboda and S. M. Block. Biological applications of optical forces. *Annu. Rev. Biophys. Biomol. Struct.*, 23:247–285, 1994.

[7] R. M. Simmons, J. T. Finer, S. Chu, and J. A. Spudich. Quantitative measurements of force and displacement using an optical trap. *Biophys. J.*, 70:1813–1822, 1996.

[8] K Visscher, M J Schnitzer, and S M Block. Single kinesin molecules studied with a molecular force clamp. *Nature*, 400:184–189, 1999.

[9] J. S. Meiners and S. R. Quake. Femtonewton force spectroscopy of single extended DNA molecules. *Phys. Rev. Lett.*, 84:5014–5017, 2000.

[10] J. W. Shaevitz, E. A. Abbondanzieri, R. Landick, and S. M. Block. Backtracking by single rna polymerase molecules observed at near-base-pair resolution. *Nature*, 426, 2003.

[11] E. A. Abbondanzieri, W. J. Greenleaf, J. W. Shaevitz, R. Landick, and S. M. Block. Direct observation of base-pair stepping by rna polymerase. *Nature*, 438:460–465, 2005.

[12] A Rohrbach. Switching and measuring a force of 25 femtonewtons with an optical trap. *Opt. Express*, 13:9695–9701, 2005.

[13] G. Binning, C. F. Quate, and C. Gerber. Atomic force microscope. *Phys. Rev. Lett.*, 56:930–933, 1986.

[14] W. A. Ducker, T. J. Senden, and R. M. Pashley. Direct measurement of colloidal forces using an atomic force microscope. *Nature*, 353:239–241, 1991.

[15] V. G. Zarnitsyn and A. G. Fedorov. Mechanosensing using drag force for imaging soft biological membranes. *Langmuir*, 2007.

[16] J. Leach, S. Keen, M. J. Padgett, C. Saunter, and G. D. Love. Direct measurement of the skew angle of the poynting vector in a helically phased beam. *Optics Express*, 14:11919–11924, 2006.

[17] S. Keen, J. Leach, G. Gibson, and M. J. Padgett. Comparison of a high-speed camera and a quadrant detector for measuring displacements in optical tweezers. *Journ. of Opt. A-Pure And Appl. Opt.*, 9:S264–S266, 2007.

[18] E. Eriksson, S. Keen, J. Leach, M. Goksor, and M. J. Padgett. The effect of external forces on discrete motion within holographic optical tweezers. *Optics Express*, 15:18268–18274, 2007.

[19] R. Di Leonardo, S. Keen, F. Ianni, J. Leach, M. J. Padgett, and G. Ruocco. Hydrodynamic interactions in two dimensions. *Phys. Rev. E: Stat., Nonlinear, Soft Matter Phys.*, 78:031406, 2008.

[20] R. Di Leonardo, S. Keen, J. Leach, C. D. Saunter, G. D. Love, G. Ruocco, and M. J. Padgett. Eigenmodes of a hydrodynamically coupled micron-size multiple-particle ring. *Phys. Rev. E: Stat., Nonlinear, Soft Matter Phys.*, 76:061402, 2007.

[21] J. Molloy and M. J. Padgett. Lights, action: optical tweezers. *Contemp. Phys.*, 43:241–258, 2002.

[22] F. Gittes and C. Schmidt. Interference model for back-focal-plane displacement detection in optical tweezers. *Opt. Lett.*, 23:7–9, 1998.

[23] M. W. Allersma, F. G., M. J. de Castro, R. J. Stewart, and C. F. Schmidt. Two-dimensional tracking of ncd motility by back focal plane interferometry. *Biophys. J.*, 74:10741085, 1998.

[24] A. Pralle, M. Prummer, E. L. Florin, E. H. K. Stelzer, and J. K. H. Horber. Three-dimensional high-resolution particle tracking for optical tweezers by forward scattered light. *Microscopy Research And Technique*, 44:378–386, 1999.

[25] J. S. Meiners and S. Quake. Direct measurement of hydrodynamic cross correlations between two particles in an external potential. *Phys. Rev. Lett.*, 82:2211–2214, 1999.

[26] J. H. G. Huisstede, K. O. van der Werf, M. L. Bennink, and V. Subramaniam. Force detection in optical tweezers using backscattered light. *Optics Express*, 13:1113–1123, 2005.

[27] S F Tölic-Norrelykke, E Schäffer, J Howard, F S Pavone, F Jülicher, and H Flyvbjerg. Calibration of optical tweezers with positional detection in the back focal plane. *Rev. of Sci. Instrum.*, 77, 2006.

[28] K. Berg-Sörensen and H. Flyvbjerg. Power spectrum analysis for optical tweezers. *Rev of Sci. Instrum.*, 75:594–612, 2004.

[29] J. Happel and H. Brenner. *Low Reynolds number hydrodynamics*. Kluwer Academic Publishers, 1983.

[30] R. Kubo, M. Toda, and N. Hashitsume. *Statistical Physics*. Heidelberg: Springer, 1985.

[31] A. Pralle, E. L. Florin, E. H. K. Stelzer, and J. K. H. Horber. Local viscosity probed by photonic force microscopy. *Applied Physics A-Materials Science & Processing*, 66:S71–S73, 1998.

[32] I. M. Tolic-Norrelykke, K. Berg-Sorensen, and H. Flyvbjerg. Matlab program for precision calibration of optical tweezers. *Comp. Phys Comm.*, 159:225–240, 2004.

[33] D. W. Allan. Statistics of atomic frequency standards. *Proc. IEEE*, 54:221–230, 1966.

[34] G. M. Gibson, J. Leach, S. Keen, A. J. Wright, and M. J. Padgett. Measuring the accuracy of particle position and force in optical tweezers using high-speed video microscopy. *Opt. Express*, 16:14561–14570, 2008.

[35] K. Visscher, G. J. Brakenhoff, and J. J. Krol. Micromanipulation by multiple optical traps created by a single fast scanning trap integrated with the bilateral confocal scanning laser microscope. *Cytometry*, 14:105–114, 1993.

[36] K. Vermeulen, J. van Mameren, G. Stienen, E. Peterman, G. Wuite, and C. Schmidt. Calibrating bead displacements in optical tweezers using acousto-optic deflectors. *Rev. of Sci. Instrum.*, 77, 2006.

[37] E. R. Dufresne and D. G. Grier. Optical tweezer arrays and optical substrates created with diffractive optics. *Rev of Sci. Instrum.*, 69:1974–1977, 1998.

[38] E. Dufresne, G. Spalding, M. Dearing, S. Sheets, and D. Grier. Computer-generated holographic optical tweezers arrays. *Rev. Sci. Instrum.*, 72:1820–1816, 2001.

[39] J. Liesener, M. Reicherter, T. Haist, and H. J. Tiziani. Multi-functional optical tweezers using computer-generated holograms. *Opt. Commun.*, 185:77–82, 2000.

[40] C. Maurer, A. Jesacher, S. Fürhapter, S. Bernet, and M. Ritsch-Marte. Tailoring of arbitrary optical vector beams,. *New J. Phys.*, 9:78, 2007.

[41] M. Reicherter, S. Zwick, T. Haist, C. Kohler, H. Tiziani, and W. Osten. Fast digital hologram generation and adaptive force measurement in liquid-crystal-display-based holographic tweezers. *Applied Optics*, 45:888–896, 2006.

[42] J. Leach, G. Sinclair, P. Jordan, J. Courtial, M. J. Padgett, J. Cooper, and Z. J. Laczik. 3d manipulation of particles into crystal structures using holographic optical tweezers. *Optics Express*, 12:220–226, 2004.

[43] G. Sinclair, P. Jordan, J. Courtial, M. Padgett, J. Cooper, and Z. J. Laczik. Assembly of 3-dimensional structures using programmable holographic optical tweezers. *Opt. Express*, 12:5475–5480, 2004.

[44] Y. Roichman and D. G. Grier. Holographic assembly of quasicrystalline photonic heterostructures. *Opt. Express*, 13:5434–5439, 2005.

[45] N. B. Simpson, L. Allen, and M. J. Padgett. Optical tweezers and optical spanners with Laguerre-Gaussian modes. *J. Mod. Opt.*, 43:2485–2491, 1996.

[46] J. Leach, K. Wulff, G. Sinclair, P. Jordan, J. Courtial, L. Thomson, G. Gibson, K. Karunwi, J. Cooper, Z. J. Laczik, and M. J. Padgett. Interactive approach to optical tweezers control. *Appl. Opt.*, 45:897–903, 2006.

[47] R. Di Leonardo, F. Ianni, and G. Ruocco. Computer generation of optimal holograms for optical trap arrays. *Opt. Express*, 15:1913–1922, 2007.

[48] J. E. Curtis, B. A. Koss, and D. G. Grier. Dynamic holographic optical tweezers. *Optics Communications*, 207:169, 2002.

[49] G. Sinclair, P. Jordan, J. Leach, M. J. Padgett, and J. Cooper. Defining the trapping limits of holographical optical tweezers. *Journ. of Mod. Opt.*, 51:409–414, 2004.

[50] J. W. Hardy. *Adaptive Optics for Astronomical Telescopes*. Oxford University Press, 1998.

[51] D. G. Grier. A revolution in optical manipulation. *Nature*, 424:810–816, 2003.

[52] A. T. O'Neil, I. MacVicar, L. Allen, and M. J. Padgett. Intrinsic and extrinsic nature of the orbital angular momentum of a light beam. *Phys. Rev. Lett.*, 88, 2002.

[53] L. Allen, M. J. Padgett, and M. Babiker. The orbital angular momentum of light. In *Progress in Optics, vol xxxix*. Elsevier Science Publ B V, 1999.

[54] M. Padgett, J. Courtial, and L. Allen. Light's orbital angular momentum. *Physics Today*, 57:35–40, 2004.

[55] M. Harris, C. A. Hill, and J. M. Vaughan. Optical helices and spiral interference-fringes. *Optics Communications*, 106:161–166, 1994.

[56] M. J. Padgett and L. Allen. The poynting vector in laguerre-gaussian laser modes. *Opt. Commun.*, 121:36–40, 1995.

[57] L. Allen and M. J. Padgett. The poynting vector in laguerre-gaussian beams and the interpretation of their angular momentum density. *Opt. Commun.*, 184:67–71, 2000.

[58] J. Arlt. Handedness and azimuthal energy flow of optical vortex beams. *J. Mod. Opt.*, 50:1573–1580, 2003.

[59] H. I. Sztul and R. R. Alfano. Double-slit interference with Laguerre-Gaussian beams. *Opt. Express*, 31:999–1001, 2006.

[60] V. Y. Bazhenov, M. V. Vasnetsov, and M. S. Soskin. Laser-beams with screw dislocations in their wave-fronts. *JETP Lett.*, 52:429–431, 1990.

[61] L. Allen, M. W. Beijersbergen, R. J. C. Spreeuw, and J. P. Woerdman. Orbital angular-momentum of light and the transformation of laguerre-gaussian laser modes. *Phys. Rev. A: At., Mol., Opt. Phys.*, 45:8185–8189, 1992.

[62] W. H. Southwell. Wave-front estimation from wave-front slope measurements. *Journal Of The Optical Society Of America*, 70:998–1009, 1980.

[63] I. V. Basistiy, V. V. Slyusar, M. S. Soskin, M. V. Vasnetsov, and A. Y. Bekshaev. Manifestation of the rotational doppler effect by use of an off-axis optical vortex beam. *Opt. Lett.*, 28:1185–1187, 2003.

[64] J. Courtial, K. Dholakia, L. Allen, and M. J. Padgett. Gaussian beams with very high orbital angular momentum. *Opt. Commun.*, 144:210–213, 1997.

[65] C. A. Alonzo, P. J. Rodrigo, and J. Gluckstad. Helico-conical optical beams: a product of helical and conical phase fronts. *Opt. Express*, 13:1749–1760, 2005.

[66] A. Ashkin, J. M. Dziedzic, J. E. Bjorkholm, and S. Chu. Observation of a single-beam gradient force optical trap for dielectric particles. *Opt. Lett.*, 11:288–290, 1986.

[67] J. C. Crocker and D. G. Grier. Methods of digital video microscopy for colloidal studies. *J. Colloid Interface Sci.*, 179:1505–1512, 1996.

[68] B. C. Carter, G. T. Shubeita, and S. P. Gross. Tracking single particles: a user-friendly quantitative evaluation. *Physical Biology*, 2:60–72, 2005.

[69] O. Otto, C. Gutsche, F. Kremer, and U. F. Keyser. Optical tweezers with 2.5khz bandwidth video detection for single-colloid electrophoresis. *Rev. Sci. Instrum.*, 79:023710, 2008.

[70] K. Visscher, S. P. Gross, and S. M. Block. Construction of multiple-beam optical traps with nanometer-resolution position sensing. *IEEE Journal of Selected Topics in Quantum Electronics*, 2, 1996.

[71] R. Larson. *The Structure and Rheology of Complex Fluids*. Oxford University Press, 1999.

[72] P. Jordan, J. Leach, M. Padgett, P. Blackburn, N. Isaacs, M. Goksor, D. Hanstorp, A. Wright, J. Girkin, and J. Cooper. Creating permanent 3D arrangements of isolated cells using holographic optical tweezers. *Lab on a Chip*, 5:1224–1228, 2005.

[73] G. M. Akselrod, W. Timp, U. Mirsaidov, Q. Zhao, C. Li, R. Timp, K. Timp, P. Matsudaira, and G. Timp. Laser-guided assembly of heterotypic three-dimensional living cell microarrays. *Biophys. J.*, 91:3465–3473, 2006.

[74] R. Di Leonardo, J. Leach, H. Mushfique, J. M. Cooper, G. Ruocco, and M. J. Padgett. Multipoint holographic optical velocimetry in microfluidic systems. *Phys. Rev. Lett.*, 96:134502, 2006.

[75] E. Eriksson, J. Scrimgeour, A. Graneli, K. Ramser, R. Wellander, J. Enger, D. Hanstrop, and M. Goksor. Optical manipulation and microfluidics for studies of single cell dynamics. *JOPA*, 9:S113–S121, 2007.

[76] E. Eriksson, E. Jonas, B. Nordlander, N. Erjavec, K. Ramser, M. Goksor, S. Hohmann, T. Nystrom, and D. Hanstorp. A microfluidic system in combination with optical tweezers for analyzing rapid and reversible cytological alterations in single cells upon environmental changes. *Lab on a chip*, 7:71–76, 2007.

[77] C. H. J. Schmitz, J. P. Spatz, and J. E. Curtis. High-precision steering of multiple holographic optical traps. *Opt. Express*, 13:8678–8685, 2005.

[78] A. Ashkin. Forces of a single-beam gradient laser trap on a dielectric sphere in the ray optics regime. *Biophys. J.*, 61:569–582, 1992.

[79] M. P. MacDonald, G. C. Spalding, and K. Dholakia. Microfluidic sorting in an optical lattice. *Nature*, 425:390–398, 2003.

[80] Jr. R. W. Applegate, J. Squier, T. Vested, J. Oakey, and D. W. M. Marr. Optical trapping, manipulation, and sorting of cells and colloids in microfluidic systems with diode laser bars. *Opt. Express*, 12:4390–4398, 2004.

[81] J. Leach, H. Mushfique, R. di Leonardo, M. Padgett, and J. Cooper. An optically driven pump for microfluidics. *Lab On A Chip*, 6:735–739, 2006.

[82] H. Mushfique, J. Leach, H. Yin, R. Di. Leonardo, M. J. Padgett, and Jonathan M. Cooper. 3d mapping of microfluidic flow in laboratory-on-a-chip structures using optical tweezers. *Anal. Chem.*, 80:4237–4240, 2008.

[83] P. Cicuta and A. M. Donald. Microrheology: a review of the method and applications. *Soft Matter*, 3:1449–1455, 2007.

[84] M. A. K. Williams, R. R. Vincent, D. N. Pinder, and Y. Hemar. Microrheological studies offer insights into polysaccharide gels. *Journal Of Non-Newtonian Fluid Mechanics*, 149:63–70, 2008.

[85] T. Okajima and H. Tokumoto. Nanorheology of living cells investigated by atomic force microscopy. *Nihon Reoroji Gakkaishi*, 36:81–86, 2008.

[86] C. Wilhelm. Out-of-equilibrium microrheology inside living cells. *Phys Rev Lett*, 101, 2008.

[87] A. R. Bausch, W. Moller, and E. Sackmann. Measurement of local viscoelasticity and forces in living cells by magnetic tweezers. *Biophys. J.*, 76:573–579, 1999.

[88] R. R. Brau, J. M. Ferrer, H. Lee, C. E. Castro, B. K. Tam, P. B. Tarsa, P. Matsudaira, M. C. Boyce, R. D. Kamm, and M. J. Lang. Passive and active microrheology with optical tweezers. *JOPA*, 9:S103–S112, 2007.

[89] M. Fischer and K. Berg-Sorensen. Calibration of trapping force and response function of optical tweezers in viscoelastic media. *Journal Of Optics A-Pure And Applied Optics*, 9:S239–S250, 2007.

[90] M. Atakhorrami, J. I. Sulkowska, K. M. Addas, G. H. Koenderink, J. X. Tang, A. J. Levine, F. C. MacKintosh, and C. F. Schmidt. Correlated fluctuations of microparticles in viscoelastic solutions: Quantitative measurement of material properties by microrheology in the presence of optical traps. *Phys. Rev. E: Stat., Nonlinear, Soft Matter Phys.*, 73, 2006.

[91] G. Pesce, A. Sasso, and S. Fusco. Viscosity measurements on micron-size scale using optical tweezers. *Rev. Sci. Instrum.*, 76, 2005.

[92] A. Buosciolo, G. Pesce, and A. Sasso. New calibration method for position detector for simultaneous measurements of force constants and local viscosity in optical tweezers. *Opt. Commun.*, 230:357–368, 2004.

[93] A. Rohrbach, C. Tischer, D. Neumayer, E. Florin, and E. H. K. Stelzer. Trapping and tracking a local probe with a photonic force microscope. *Rev of Sci. Instrum.*, 75:2197–2210, 2004.

[94] B. A. Nemet and M. Cronin-Golomb. Measuring microscopic viscosity with optical tweezers as a confocal probe. *Applied Optics*, 42:1820–1832, 2003.

[95] R. Lugowski, B. Kolodziejczyk, and Y. Kawata. Application of laser-trapping technique for measuring the three-dimensional distribution of viscosity. *Opt. Commun.*, 202:1–8, 2002.

[96] S. J. Parkin, G. Knoner, T. A. Nieminen, N. R. Heckenberg, and H. Rubinsztein-Dunlop. Picoliter viscometry using optically rotated particles. *Phys. Rev. E: Stat., Nonlinear, Soft Matter Phys.*, 76:041507, 2007.

[97] C. D. Saunter, G. D. Love, M. Johns, and J. Holmes. FPGA technology for high-speed low-cost adaptive optics. *proc. SPIE*, 6018:429–435, 2005.

[98] H. Faxén. The resistance against the movement of a rigour sphere in viscous fluids, which is embedded between two parallel layered barriers. *Annalen der Physik*, 4:89, 1922.

[99] H. Faxén. *Arikiv fur Matematik Astronomi och Fysik*, 18:1, 1924.

[100] H. Tanaka and T. Araki. Simulation method of colloidal suspensions with hydrodynamic interactions: Fluid particle dynamics. *Phys. Rev. Lett.*, 85:1338–1341, 2000.

[101] M. Doi and S.F. Edwards. *The Theory of Polymer Dynamics*. Oxford University Press, 1986.

[102] J. G. de la Torre and V. A. Bloomfield. Hydrodynamic properties of complex, rigid, biological macromolecules: theory and applications. *Q. Rev. Biophys.*, 14:81, 1981.

[103] S. Hayward and N. Go. Collective variable description of native protein dynamics. *Annu. Rev. Phys. Chem.*, 46:223, 1995.

[104] M. Polin, D. G. Grier, and S. R. Quake. Anomalous vibrational dispersion in holographically trapped colloidal arrays. *Phys. Rev. Lett.*, 96:088101, 2006.

[105] R. Di Leonardo, F. Saglimbeni, and G. Ruocco. Very-long-range nature of capillary interactions in liquid films. *Phys. Rev. Lett.*, 100, 2008.

[106] E. R. Dufresne, T. M. Squires, M. P. Brenner, and D. G. Grier. Hydrodynamic coupling of two brownian spheres to a planar surface. *Phys. Rev. Lett.*, 85:3317–3320, 2000.

[107] E. R. Dufresne, D. Altman, and D. G. Grier. Brownian dynamics of a sphere between parallel walls. *Europhysics Letters*, 53:264–270, 2001.

[108] T. Savin and P. S. Doyle. Static and dynamic errors in particle tracking microrheology. *Biophys. J.*, 88:623–638, 2005.

[109] R. Omori, T. Kobayashi, and A. Suzuki. Observation of a single-beam gradient-force optical trap for dielectric particles in air. *Opt. Lett.*, 22:816–8, 1997.

[110] D. R. Burnham and D. McGloin. Holographic optical trapping of aerosol droplets. *Opt. Express*, 14:4175–4181, 2006.

[111] J. F. Brady and G. Bossis. Stokesian dynamics. *Annual Review Of Fluid Mechanics*, 20:111–157, 1988.

[112] R. W. Gerchberg and W. O. Saxton. Holography without fringes in electron-microscope. *Optik Jena*, 35:237, 1972.

[113] J. Monteith and M. Unsworth. *Principles of Environmental Physics.* Academic Press, 2008.

[114] G. R. Fowles. *Analytical Mechanics.* Saunders College Publishing: Philadelphia, 1986.

[115] P.W. Anderson. *Basic Notions of Condensed Matter Physics.* Perseus Publishing, 1997.

[116] G.K. Batchelor. *An Introduction to Fluid Dynamics.* Cambridge University Press, 1967.

[117] Xiao-Lun Wu and Albert Libchaber. Particle diffusion in a quasi-two-dimensional bacterial bath. *Phys. Rev. Lett.*, 84:3017–3020, 2000.

[118] P. G. Saffman. Brownian-motion in thin sheets of viscous-fluid. *Journal Of Fluid Mechanics*, 73:593–602, 1976.

[119] C. Cheung, Y.H. Hwang, X l. Wu, and H.J. Choi. Diffusion of particles in free-standing liquid films. *Phys. Rev. Lett.*, 76:2531, 1996.

[120] B. Cui, H. Diamant, B. Lin, and S.A. Rice. Anomalous hydrodynamic interaction in a quasi-two-dimensional suspension. *Phys. Rev. Lett.*, 92:258301, 2004.

[121] R. Di Leonardo, F. Saglimbeni, and G. Ruocco. Very-long-range nature of capillary interactions in liquid films. *Physical Review Letters*, 100:106103, 2008.

[122] A. J. Banchio, J. Gapinski, A. Patkowski, W. Haussler, A. Fluerasu, S. Sacanna, P. Holmqvist, G. Meier, M. P. Lettinga, and G. Nagele. Many-body hydrodynamic interactions in charge-stabilized suspensions. *Phys. Rev. Lett.*, 96:138303, 2006.

[123] A. Ramirez-Saito, C. Bechinger, and J. C. Arauz-Lara. Optical microscopy measurement of pair correlation functions. *Phys. Rev. E: Stat., Nonlinear, Soft Matter Phys.*, 74:030401, 2006.